



AMERICAN METEOROLOGICAL SOCIETY

Journal of the Atmospheric Sciences

EARLY ONLINE RELEASE

This is a preliminary PDF of the author-produced manuscript that has been peer-reviewed and accepted for publication. Since it is being posted so soon after acceptance, it has not yet been copyedited, formatted, or processed by AMS Publications. This preliminary version of the manuscript may be downloaded, distributed, and cited, but please be aware that there will be visual differences and possibly some content differences between this version and the final published version.

The DOI for this manuscript is doi: 10.1175/JAS-D-12-039.1

The final published version of this manuscript will replace the preliminary version at the above DOI once it is available.

If you would like to cite this EOR in a separate work, please use the following full citation:

Yang, P., L. Bi, B. Baum, K. Liou, G. Kattawar, M. Mishchenko, and B. Cole, 2012: Spectrally consistent scattering, absorption, and polarization properties of atmospheric ice crystals at wavelengths from 0.2 μm to 100 μm . *J. Atmos. Sci.* doi:10.1175/JAS-D-12-039.1, in press.



1 **Spectrally consistent scattering, absorption, and polarization**
2 **properties of atmospheric ice crystals at wavelengths**
3 **from 0.2 μm to 100 μm**
4
5
6

7 Ping Yang,¹ Lei Bi,¹ Bryan A. Baum,²

8
9 Kuo-Nan Liou,³ George W. Kattawar,⁴ Michael I. Mishchenko,⁵ Benjamin Cole¹
10
11
12
13

- 14 1. Department of Atmospheric Sciences, Texas A&M University, College Station,
15 TX 77843, USA
- 16 2. Space Science and Engineering Center, University of Wisconsin-Madison,
17 Madison, WI 53706, USA
- 18 3. Joint Institute for Earth System Science and Engineering, and Department of
19 Atmospheric and Oceanic Sciences, University of California, Los Angeles, CA
20 90095, USA
- 21 4. Department of Physics & Astronomy, Texas A&M University, College Station,
22 TX 77843, USA
- 23 5. NASA Goddard Institute for Space Studies, 2880 Broadway, New York, NY
24 10025, USA
25
26
27
28
29

For publication in the

30 *Journal of the Atmospheric Sciences*
31
32
33
34
35

36 * Corresponding author address: Prof. Ping Yang, Department of Atmospheric Sciences,
37 Texas A&M University, College Station, TX 77843; Email: pyang@tamu.edu
38
39

Abstract

40
41
42
43
44
45
46
47
48
49
50
51
52
53
54
55
56
57
58
59
60
61
62
63
64

A data library is developed containing the scattering, absorption, and polarization properties of ice particles in the spectral range from 0.2 μm to 100 μm . The properties are computed based on a combination of the Amsterdam discrete dipole approximation (ADDA), the T-matrix method, and the improved geometric-optics method (IGOM). The electromagnetic edge effect is incorporated into the extinction and absorption efficiencies computed from the IGOM. A full set of single-scattering properties is provided by considering three-dimensional random orientations for 11 ice crystal habits: droxtals, prolate spheroids, oblate spheroids, solid and hollow columns, compact aggregates composed of 8 solid columns, hexagonal plates, small spatial aggregates composed of 5 plates, large spatial aggregates composed of 10 plates, and solid and hollow bullet rosettes. The maximum dimension of each habit ranges from 2 μm to 10,000 μm in 189 discrete sizes. For each ice crystal habit, three surface roughness conditions (i.e., smooth, moderately roughened, and severely roughened) are considered to account for the surface texture of large particles in the IGOM applicable domain. The data library contains the extinction efficiency, single-scattering albedo, asymmetry parameter, six independent non-zero elements of the phase matrix (P_{11} , P_{21} , P_{22} , P_{33} , P_{43} , and P_{44}), particle projected area, and particle volume to provide the basic single-scattering properties for remote sensing applications and radiative transfer simulations involving ice clouds. Furthermore, a comparison of satellite observations and theoretical simulations for the polarization characteristics of ice clouds demonstrates that ice cloud optical models assuming severely roughened ice crystals significantly outperform their counterparts assuming smooth ice crystals.

65 **1. Introduction**

66
67 Numerous studies have elaborated on the important role natural ice clouds and
68 contrails play in the atmospheric radiation budget essential to weather and climate
69 systems (see Liou, 1986; Lynch et al., 2002; Baran, 2009; Yang et al., 2010; and
70 references cited therein). The single-scattering properties of ice crystals are fundamental
71 to the development of a variety of applications involving these clouds. For example, the
72 properties are indispensable in both the computation and parameterization of the bulk
73 broadband radiative properties of ice clouds (Fu et al., 1998; McFarquhar et al., 2002;
74 Key et al., 2002; Gu et al., 2003; Edwards et al., 2007; Liou et al., 2008), in radiative
75 transfer simulations (Mayer and Kylling, 2005), and in assessing the radiative forcing of
76 ice clouds (Wendisch et al., 2007; Edwards et al., 2007). For operational retrievals, the
77 single-scattering properties are averaged over various particle size distributions with an
78 assumed habit prescription (Baum et al., 2005, 2011; Yue et al., 2007; Baran, 2009). The
79 resulting bulk scattering properties are used in radiative transfer models to simulate the
80 reflectance and transmittance associated with ice clouds over a range of conditions, and
81 are tabulated in look-up tables (LUTs) for use in subsequent data reduction to infer ice
82 cloud optical thickness and effective particle size from airborne or satellite observations
83 (Platnick et al., 2003; King et al., 2004; Huang et al., 2004; Wang et al., 2009; Minnis et
84 al., 2011). The need for consistency in the optical properties over a wide spectral range
85 becomes evident when comparing retrievals from sensors taking measurements with quite
86 different methods such as solar wavelength techniques, polarization techniques, or
87 infrared wavelength techniques (e.g., Baran and Francis, 2004; Ham et al., 2009; Zhang
88 et al., 2009).

89 The single-scattering properties for individual ice habits have been reported in
90 numerous articles by Wendling et al. (1979), Cai and Liou (1982), Takano and Liou
91 (1989, 1995), Muinonen (1989), Macke (1993), Macke et al. (1996a), Yang and Liou
92 (1996a,b), Sun et al. (1999), Havemann and Baran (2001), Baran et al. (2001), Borovoi et
93 al. (2002), Hesse and Ulanowski (2003), Um and McFarquhar (2007), and Nakajima et
94 al. (2009). Moreover, several previous studies have developed ice particle single-
95 scattering properties in relatively limited domains. For example, using a ray-tracing
96 model developed by Wendling et al. (1979) with some enhancements, Hess and Wiegner
97 (1994) and Hess et al. (1998) created a single-scattering property database for hexagonal
98 ice columns and plates at 12 wavelengths from the ultraviolet (UV) to the infrared (IR)
99 spectral region. Yang et al. (2000) developed the single-scattering properties in the solar
100 spectrum from 0.2 μm to 5 μm for six ice particle habits: plates, columns, hollow
101 columns, planar bullet rosettes with four branches, three-dimensional (3D) bullet rosettes
102 with six branches, and compact aggregates of solid columns. Yang et al. (2005) published
103 a database for droxtals, plates, columns, hollow columns, 3D bullet rosettes, and compact
104 aggregates of columns at 49 discrete wavelengths between 3 μm and 100 μm . The single-
105 scattering properties were calculated by a combination of two scattering computational
106 models: the finite-difference time domain method (FDTD) (Yee, 1966; Yang and Liou,
107 1996a; Sun et al., 1999) and the IGOM (Yang and Liou, 1996b).

108 The data libraries presented by Yang et al. (2000; 2005) contained several
109 inconsistencies in the solar and thermal infrared (IR) spectral regions due to differences
110 in the particle shapes and the computational methodologies used in the computations. An
111 empirical approach known as the composite method (Fu et al., 1998), which partially uses

112 the concept of “equivalent” spheres for nonspherical particles, was employed to merge
113 the extinction and absorption efficiencies in the size parameter region of overlapping
114 FDTD and IGOM results in the IR database (Yang et al., 2005). The inconsistencies were
115 also generated from different discretizations of the particle size bins employed in the
116 solar and IR regions and from slightly different particle aspect ratios for some habits.
117 Additionally, in Yang et al. (2000), the intensity (P_{11} component) contained an artificial
118 term referred to as the delta transmission (Takano and Liou, 1989; Mishchenko and
119 Macke, 1998), which resulted from either the conventional geometric optics method (Cai
120 and Liou, 1982; Takano and Liou, 1989) or a simplification in the IGOM related to the
121 treatment of the forward peak in the phase function for large particles. The delta
122 transmission term produced complications in radiative transfer simulations as well as in
123 the interpretation of the effective optical thickness of ice clouds.

124 This study is intended to develop a spectrally consistent data library containing the
125 scattering, absorption, and polarization properties of a set of 11 randomly oriented ice
126 crystal habits at wavelengths from 0.2–100 μm . The maximum diameters for each habit
127 range from 2 to 10,000 μm . The ice particle habits include quasi-spherical particles
128 (droxtals, prolate spheroids, and oblate spheroids), hexagonal plates, solid and hollow
129 hexagonal columns, small and large spatial aggregates of plates defined following Xie et
130 al. (2011), compact aggregates of solid columns, and solid and hollow 3D bullet rosettes
131 (Yang et al., 2008a). The data library provides information relating to the volume and
132 projected area of each habit as well as the asymmetry parameter, single-scattering albedo,
133 extinction and absorption cross sections/efficiencies, and the six nonzero elements of the
134 phase matrix.

135 The new data library presented in this paper provides the basic and consistent single-
136 scattering data for a selection of ice crystal sizes and shapes observed in the atmosphere.
137 The library adds to previous work regarding the derivation of ice particle optical
138 properties in the following four ways: (1) the scattering models used to solve for the
139 various ice particle optical properties have been improved (e.g., Yang et al., 2008a; Yang
140 and Liou, 2009a,b; Bi et al., 2008, 2011a,b; Liou et al., 2010, 2011) since the publication
141 of the previous databases (Yang et al., 2000, 2005), and, at the same time, the unphysical
142 delta-transmission feature has been removed by means of a new approach (Bi et al.,
143 2008); (2) the calculations employ the real and imaginary indices of refraction for ice
144 presented by Warren and Brandt (2008) to conduct the necessary single-scattering and
145 polarization calculations; (3) the aspect ratios used in the calculations are consistent for a
146 spectral range from 0.2 μm to 100 μm ; (4) the composite method (Fu et al., 1998) was
147 not adopted to merge the scattering properties at size parameters when the ADDA and
148 IGOM solutions overlap, but a new approach was developed that includes the edge effect
149 for the extinction efficiency and the above/below edge effect for the absorption efficiency
150 (Nussenzveig and Wiscombe, 1980; Baran and Havemann 1999) in the IGOM solutions.
151 With the new approach, the results for the extinction and absorption efficiencies are
152 continuous as functions of the size parameter (x) proportional to the ratio of the particle
153 circumference to the incident wavelength, regardless of whether the properties are
154 computed from the ADDA or IGOM. In this study, the T-matrix method (Mishchenko et
155 al., 1996) was used for prolate and oblate spheroids that may approximate the shapes of
156 small ice crystals in aircraft contrails (Mishchenko and Sassen, 1998; Iwabuchi et al.,
157 2012). While quasi-spherical particles are sometimes observed in images from cloud

158 probes, perhaps due to insufficient optical resolution, the underlying ice crystal
159 morphology can be more complex (Connolly et al. 2007). Calculations for other faceted
160 habits are performed using the ADDA computational program (Yurkin et al., 2007a;
161 <http://code.google.com/p/a-dda/downloads/list>) for $x \leq 20$ and an improved and refined
162 version of the IGOM (Bi et al., 2009) for $x > 20$. Because no single model among the
163 existing electromagnetic scattering computational methods (Mishchenko et al., 2000;
164 Kahnert, 2003; Wriedt, 2009) can be employed over the entire range of size parameters
165 and habits, significant effort was required to merge the ADDA and IGOM solutions as
166 seamlessly as possible.

167 The paper is organized as follows: Section 2 explains the methodology for the
168 development of the single-scattering data library; Section 3 illustrates the single-
169 scattering properties of a number of ice crystal habits; and Section 4 summarizes the
170 present work.

171

172 **2. Methodology**

173

174 In our calculations, we used the most recent compilation of the refractive index of
175 ice (Warren and Brandt, 2008) from 0.2 μm to 100 μm . Fig. 1a shows the imaginary part
176 (m_i) of the ice refractive index versus the corresponding real part (m_r), while Fig. 1b and
177 1c respectively show the variations of m_i and m_r as functions of wavelength. In Fig. 1a,
178 the open circle symbols signify the 445 spectral points chosen for the detailed scattering
179 computations. As illustrated in Figs. 1b and 1c, the spectral points for the refractive index
180 were selected at the maxima and minima of either m_i or m_r . Extensive sensitivity studies,
181 using spheres, were performed to ensure that the optical properties at wavelengths not

182 coinciding with the selected spectral points could be obtained via interpolation and with
183 negligible errors by using the properties at two nearby spectral points.

184 The left and right panels in Fig. 2 respectively show the grid points selected for
185 particle size and wavelength in the computational domain of the previous datasets (Yang
186 et al., 2000, 2005) and the present library. As shown in the left panel, fewer particle size
187 bins were selected in the solar spectral region (Yang et al., 2000) than in the IR spectral
188 region (Yang et al., 2005). This inconsistency is circumvented by the present selection of
189 particle sizes shown in the right panel of Fig. 2. In this study, 189 points are selected for
190 particle sizes ranging from 2 μm to 10,000 μm ; whereas, only 24 sizes between 3 μm to
191 3500 μm were used in Yang et al. (2000) and only 45 sizes between 2 μm to 10,000 μm
192 were used in Yang et al. (2005).

193 In situ measurements have indicated ice crystals to have predominantly hollow
194 structures (Walden et al., 2003, Schmitt and Heymsfield, 2007), which affected the
195 choice of ice crystal habits considered in this study and shown in Fig. 3. The first row
196 shows quasi-spherical ice crystals (droxtal, prolate spheroid, and oblate spheroid); the
197 second row shows solid and hollow hexagonal columns and compact aggregates of
198 hexagonal columns; the third row shows hexagonal plates and spatial aggregates of
199 hexagonal plates; and the fourth row shows solid and hollow bullet rosettes. In addition
200 to the variety of habits shown in Fig. 3, the effect of surface roughness is considered in
201 the current IGOM calculations. As a proxy to mimic particle surface roughness, the
202 surface slope is distorted randomly for each incident ray. Similar to the approach
203 suggested by Cox and Munk (1954) for defining the roughness conditions of the sea
204 surface, a normal distribution of the surface slope for a particle's surface is defined by

205
$$P(Z_x, Z_y) = \frac{1}{\sigma^2 \pi} \exp \left[-\frac{Z_x^2 + Z_y^2}{\sigma^2} \right] \quad (1)$$

206 where Z_x and Z_y indicate the local slope variations of the particle's surface along two
 207 orthogonal directions, i.e., the x and y directions. The parameter σ is associated with the
 208 degree of surface roughness with larger values of σ denoting rougher particle surfaces. In
 209 the present simulations, three values for σ are chosen: $\sigma=0$ (smooth surface); $\sigma=0.03$
 210 (moderate surface roughness); and, $\sigma=0.5$ (severe surface roughness). Yang and Liou
 211 (1998) provide a more complete description of the surface slopes incorporated into the
 212 IGOM.

213 Table 1 provides the aspect ratios of the ice crystal habits shown in Fig. 3. In the
 214 case of an aggregate of columns or plates, the semi-width (a) and length (L) of each
 215 hexagonal element of the aggregate are on a relative scale, the center of the element in
 216 the particle system is denoted by three coordinates (X_o, Y_o, Z_o), and the orientation of the
 217 element is specified in terms of three Euler angles (α, β, γ) with Z-Y-Z rotations. For
 218 columns, plates, and droxtals, the aspect ratios used are from the literature (Arnott et al.,
 219 1994; Auer and Veal, 1970; Mitchell and Arnott, 1994; Pruppacher and Klett, 1980;
 220 Yang et al., 2003; Zhang et al., 2004) and are similar to those used by Yang et al. (2000,
 221 2005). The geometries of solid and hollow bullet rosettes used are the same as those
 222 defined in Yang et al. (2000, 2008a). With the aspect ratio relationship defined in Table 1
 223 for a solid or hollow bullet rosette with a given maximum dimension of D , the length (L)
 224 of the columnar portion of a bullet branch can be obtained by solving the following
 225 nonlinear equation:

226
$$4L^2 + 15.0532L^{1.63} + 19.4987L^{1.26} = D^2, \quad (2)$$

227 As in Yang et al. (2000, 2005), ice crystals are assumed to be randomly oriented
 228 in space with an equal number of mirror positions. In this case, the 4x4 phase matrix has
 229 six independent elements (van de Hulst, 1957; Bohren and Huffman, 1983; Liou, 2002;
 230 Mishchenko et al., 2002). Specifically, the incident and scattered Stokes parameters,
 231 (I_i, Q_i, U_i, V_i) and (I_s, Q_s, U_s, V_s) , are related as follows:

$$232 \begin{bmatrix} I_s \\ Q_s \\ U_s \\ V_s \end{bmatrix} = \frac{\sigma_s}{4\pi r^2} \begin{bmatrix} P_{11} & P_{12} & 0 & 0 \\ P_{12} & P_{22} & 0 & 0 \\ 0 & 0 & P_{33} & P_{34} \\ 0 & 0 & -P_{34} & P_{44} \end{bmatrix} \begin{bmatrix} I_i \\ Q_i \\ U_i \\ V_i \end{bmatrix}, \quad (3)$$

233 where σ_s is the scattering cross section and r is the distance between the scattering
 234 particle and the point of observation. In the current data library, all the nonzero phase
 235 matrix elements in Eq. (3) are included and the phase matrix is a function of the
 236 scattering angle and invariant with the azimuthal angle.

237 In Yang et al. (2005), the FDTD method was applied to small size parameters
 238 ($x \leq 20$); however, we have used the ADDA for application to this size parameter range.
 239 The FDTD is based on the time-dependent Maxwell equations; whereas, the ADDA
 240 solves the electromagnetic scattering problem involving a dielectric particle in the
 241 frequency domain. Although the FDTD and ADDA differ substantially from a
 242 computational perspective, their numerical solutions are consistent. As an example, Fig. 4
 243 shows the nonzero phase matrix elements of randomly oriented hexagonal columns at
 244 two wavelengths, 0.66 μm and 12 μm . The orientation of the particle is specified through
 245 Euler angles (α, β, γ) in the common Z-Y-Z convention. In Fig. 4, the phase matrix is
 246 averaged using 128 α angles, 17 β angles, and 3 γ angles. For each FDTD and ADDA
 247 simulation (51 total in terms of the β and γ dependence), the phase matrix is averaged

248 through 128 scattering planes. Excellent agreement between the FDTD solution and its
249 ADDA counterpart is clearly shown in the figure. Yurkin et al. (2007b) investigated the
250 computational efficiency of the FDTD and ADDA techniques for nonabsorbing particles
251 and found the ADDA to be more efficient than the FDTD when the refractive index is
252 smaller than 1.4; however, the opposite was found for larger values of the refractive
253 index. Because the FDTD and ADDA yield the same numerical results for the spectrum
254 considered in this study, the choice between the two methods is primarily a matter of
255 computational time. The ADDA method is used for small size parameters regardless of
256 the value of the refractive index at a selected wavelength.

257 In the ADDA simulations, the number of dipoles per wavelength (labeled “dpl” in
258 the software) is a critical computational parameter that controls numerical accuracy. Two
259 criteria were used to set up this parameter: (a) $dpl > 10 |m|$, where m is the refractive
260 index; and (b) the dpl should be sufficiently large to approximately represent particle
261 geometry. For complex particle geometries, criterion (a) is insufficient for representing
262 particle geometry through dipoles and may cause shape errors. The number of
263 orientations is another parameter that impacts the accuracy of orientation-averaged
264 single-scattering properties. The ADDA employs the Romberg integration technique
265 (Davis and Rabinowitz, 1975) to perform the orientation-average with a prescribed
266 accuracy. Fig. 5 shows the number of orientations specified in the ADDA simulations for
267 solid hexagonal columns at four representative wavelengths with a prescribed accuracy of
268 10^{-5} . The number of ADDA simulations depends on the number of discretized angles of β
269 and γ , and the six-fold rotational symmetry was taken into account in setting up γ . The
270 number of orientations generally increases with the size parameter. A large number of

271 orientations increases the computational load of the ADDA method and is a limiting
272 factor, although the ADDA method can handle a moderate size parameter for a single
273 orientation.

274 We use the IGOM to perform the computations for the size parameter range
275 beyond the modeling capabilities of the ADDA. As compared with the IGOM code used
276 in Yang et al. (2005), some improvements are incorporated in the present algorithm. We
277 employ (1) a more efficient recursive ray-tracing algorithm (Bi et al., 2011b) instead of
278 the Monte-Carlo ray-tracing described in Yang and Liou (1998), (2) an improved near-to-
279 far-field mapping algorithm (Bi et al, 2009), and (3) an improved approach to account for
280 the external reflection of randomly oriented particles to reduce noise near the
281 backscattering angle (Bi et al., 2011a). For example, for convex faceted particles
282 (column, plate, and droxtal), the algorithm described in Bi et al. (2011b) is used to
283 compute the single-scattering properties for moderate size parameters.

284 Yang et al. (2005) used a composite method (Fu et al., 1998) based on a weighted
285 combination of the Lorenz-Mie and IGOM solutions to improve the accuracy of the
286 extinction and absorption efficiencies at moderate to large size parameters. In this study,
287 a physically rational approach is employed to include the edge effect on the extinction
288 efficiency and the above/below-edge effect on the absorption efficiency (van de Hulst,
289 1957; Nussenzveig and Wiscombe, 1980; Liou et al., 2010). To briefly describe the edge
290 effect, we consider the case of light scattering by a sphere in the framework of the
291 localization principle following van de Hulst (1957). With the use of the standard
292 notations for the Lorenz-Mie solution (Bohren and Huffman, 1983; Liou, 2002;

293 Mishchenko et al., 2002), the nonzero elements of the amplitude scattering matrix
 294 associated with a sphere can be written in the form

$$295 \quad S_1 = \sum_{n=1}^{\infty} \frac{2n+1}{n(n+1)} (a_n \pi_n + b_n \tau_n), \quad (4)$$

$$296 \quad S_2 = \sum_{n=1}^{\infty} \frac{2n+1}{n(n+1)} (a_n \tau_n + b_n \pi_n). \quad (5)$$

297 The n^{th} term in Eqs. (4) and (5) corresponds to a ray passing the sphere with a distance
 298 from the center of the particle of

$$299 \quad d = (n + 1/2)\lambda / 2\pi, \quad (6)$$

300 where λ is the incident wavelength. The terms with orders of $(n + 1/2) \geq x$ where x is the
 301 size parameter (i.e., ray types “a” and “b” in Fig. 6) cannot be handled within the
 302 framework of the geometric optics method, but the contribution of lower order rays (ray
 303 type “c” in Fig. 6) to the scattered radiation are taken into account. The contribution of
 304 ray types “a” and “b” to the extinction efficiency is referred to as the edge effect and
 305 given as (Nussenzveig and Wiscombe, 1980):

$$306 \quad \Delta Q_{ext,edge-effect} = \frac{1.992386}{x^{2/3}}. \quad (7)$$

307 From Eq. (7), it is evident that the edge effect decreases with an increase in the size
 308 parameter. In the geometric optics regime, the contribution of the edge effect is virtually
 309 negligible. However, in the portion of the resonance regime where the particle size is on
 310 the order of the incident wavelength, it is critical to incorporate the contribution of the

311 edge effect. In the case of the absorption efficiency, the edge effect is divided into
312 above/below edge effect (Nussenzveig and Wiscombe 1980).

313 For nonspherical particles, analytical formulations of the edge effect and the
314 above/below-edge effect cannot be derived (Liou et al., 2011). To incorporate these
315 effects into the present study, we postulate that the contributions of these effects to
316 extinction and absorption efficiencies can be semi-empirically formulated in the form

$$317 \quad \Delta Q_{ext,edge-effect} = \frac{\eta_{ext}}{(\pi D / \lambda)^{2/3}}, \quad (8)$$

$$318 \quad \Delta Q_{abs,edge-effect} = \frac{\eta_{abs}}{(\pi D / \lambda)^{2/3}}, \quad (9)$$

319 where D is the maximum dimension of a nonspherical ice crystal and the parameters η_{ext}
320 and η_{abs} are empirical coefficients. We compare the ADDA and IGOM solutions for the
321 extinction and absorption efficiencies in the resonance regime to determine the empirical
322 coefficients.

323 Unlike the conventional ray-tracing technique that assumes the extinction
324 efficiency to have a constant value (i.e., $Q_{ext} = 2$) regardless of the size parameter, the
325 IGOM is able to mimic the variation of the extinction efficiency as a function of size
326 parameter. However, the IGOM solution for Q_{ext} underestimates the particle's extinction
327 because of the exclusion of the edge effect contribution, as illustrated by comparison
328 between the ADDA and IGOM extinction efficiencies shown in Fig. 7. Note that the
329 ADDA or FDTD are rigorous numerical methods fully accounting for the edge effect.
330 The coefficient η_{ext} in Eq. (8) can be empirically determined such that the transition of
331 the ADDA solution for Q_{ext} to the IGOM counterpart is continuous. A similar approach is

332 applied to η_{abs} in Eq. (9). After the empirical addition of the edge effect to the IGOM
333 results, the resulting extinction efficiency, indicated as the “IGOM + edge effect” in Fig.
334 7, is consistent with the ADDA results for moderate size parameters. The same approach
335 is adopted to incorporate the above/below-edge effect in the computation of the
336 absorption efficiency. The efficiencies are used in the calculation of the single-scattering
337 albedo, as shown in the lower panel of Fig. 7.

338

339 **3. Results**

340

341 Based on the previous discussion, a data library was developed containing the
342 single-scattering properties for a set of 11 ice habits. These properties were computed for
343 445 wavelengths and 189 particle sizes. The database includes the six nonzero phase
344 matrix elements, extinction efficiency, asymmetry parameter, and single-scattering
345 albedo. Additionally, the projected area and volume are provided for each given particle
346 size. The phase matrix elements are computed at 498 scattering angles with an angular
347 resolution of 0.01° from 0° – 2° , 0.05° from 2° – 5° , 0.1° from 5° – 10° , 0.5° from 10° – 15° , 1°
348 from 15° – 176° , and 0.25° from 176° – 180° .

349 As an example, Fig. 8 shows the spectral variation of the integrated single-
350 scattering properties (i.e., the extinction efficiency, single-scattering albedo, and
351 asymmetry parameter) for nine ice crystal habits with a maximum diameter of $15\ \mu\text{m}$
352 ($D_{max}=15\ \mu\text{m}$). For the data shown in Fig. 8, the ice crystal surface is assumed to be
353 smooth, i.e., the parameter σ in Eq. (1) is assumed to be zero. Fig. 9 is similar to Fig. 8,
354 except for a larger size ($D_{max} = 200\ \mu\text{m}$). Figs. 8 and 9 indicate that the extinction
355 efficiency and single-scattering albedo are sensitive to ice crystal size.

356 To illustrate the integrated single-scattering properties as functions of both
357 wavelength and particle size, Fig. 10 shows contours of these properties for an spatial
358 aggregate of 10 plates (left column) and hollow bullet rosettes (right column) for
359 wavelengths from 0.2-100 μm and particle sizes from 2-10,000 μm . In the asymmetry
360 factor contours, the region marked in blue indicates the small size parameter regime,
361 while the region marked in red indicates the geometric optics regime where the
362 asymmetry factor approaches its asymptotic value. The region marked in yellow indicates
363 the resonance region in which the transition occurs from small to large size parameters;
364 note that this region is quite narrow. The variation in the extinction efficiency is strongly
365 correlated with the real part of the refractive index of ice shown in Fig. 1; whereas,
366 variation in the single-scattering albedo is sensitive to the imaginary part of the refractive
367 index.

368 Fig. 11 shows six elements of the phase matrix for the two habits in the previous
369 figure, i.e., the aggregate of 10 plates and the hollow bullet rosette. The maximum
370 dimension is 20 μm and the incident wavelength is 0.65 μm ($x \sim 97$). Fig. 12 is similar to
371 Fig. 11, except that the size is 2000 μm . Ice halos are evident in Fig. 12 for large particle
372 sizes, but are not present for the small sizes depicted in Fig. 11. However, if the
373 conventional geometric optics method (e.g., Takano and Liou, 1989) that does not
374 consider the ray spreading effect (Bi et al., 2009) is applied, halos exist for all particle
375 sizes. The dependence of the phase matrix elements on ice crystal habit is also evident in
376 Figs. 11 and 12.

377 In the data library, single-scattering properties are provided for three surface
378 roughness conditions (smooth, $\sigma=0$; moderate roughness, $\sigma=0.03$; and severe

379 roughness, $\sigma=0.5$). Baum et al. (2010) discuss the impact of roughness and ice habit on
380 the phase matrix. Further results are shown here, and Fig. 13 shows the phase function
381 and the asymmetry factor for both smooth and roughened ice crystals. The scattering
382 phase function corresponding to severe roughening is essentially featureless since the
383 scattering becomes more random, and this effect of the surface roughness on the phase
384 function has been confirmed experimentally (Barkey et al., 1999; Ulanowski et al., 2006).
385 The asymmetry factor for roughened crystals is lower than their smooth crystal
386 counterparts. A featureless phase function can be obtained numerically in several ways;
387 for example, an inclusion of air bubbles or other inhomogeneities in ice crystals provides
388 some possibilities (e.g., Macke et al., 1996b; C.-Labonnote et al., 2001).

389 For practical applications to remote sensing, the featureless phase function
390 associated with roughened ice crystals yields quite different ice cloud property retrievals
391 in comparison with smooth ice crystal retrieval results (Yang et al., 2008b; Zhang et al.
392 2009). Although the detailed nature of ice crystal surface roughness is not known from a
393 direct observational perspective, the existence of substantial ice crystal surface roughness
394 or inhomogeneity has been suggested based on indirect evidence. While the exact
395 mechanism causing the randomization of the scattering pattern is unknown, the resulting
396 featureless phase function and associated single-scattering properties can be tested using
397 polarized reflectance measurements following C.-Labonnote et al. (2001), Baran and C.-
398 Labonnote (2007), and Cole et al. (submitted). Here, we use the ice cloud polarization
399 reflectances measured by PARASOL (Polarization and Anisotropy of Reflectances for
400 Atmospheric Sciences coupled with Observations from a Lidar) to illustrate a consistency
401 test of the smooth versus roughened ice bulk scattering properties. The top panel of Fig.

402 14 shows the habit mixture used in the MODIS collection 5 ice model (Baum et al.,
 403 2005). The middle and lower panels of Fig. 14 show the bulk phase function (P_{11}) and the
 404 phase matrix element ratio $-P_{12}/P_{11}$ for smooth and severely rough ($\sigma=0.5$) conditions
 405 for an effective particle size of 50 μm based on the ice crystal habit distribution shown in
 406 the top panel. Similar to the case for individual ice crystals, the bulk optical properties for
 407 an ensemble of ice crystals are strongly dependent on particle surface texture.

408 To test the effect of surface roughness on an ice model, simulations of polarized
 409 reflectance may be compared with data from PARASOL. The polarized reflectance is
 410 defined as (C.-Labonnote et al. 2001):

411

$$412 \quad L_{nmp} = \frac{\pi(\pm\sqrt{Q^2 + U^2})}{E_s} \frac{\cos \theta_s + \cos \theta_v}{\cos \theta_s}, \quad (10)$$

413 where Q and U are the second and third Stokes parameters measured by PARASOL, E_s
 414 is solar irradiance at the top of the atmosphere, θ_s is the solar zenith angle, and θ_v is the
 415 viewing zenith angle. In Eq. (10), the sign is determined by the angle between the
 416 polarization vector and the normal to the scattering plane and the method is explained in
 417 detail by C.-Labonnote et al. (2001). To simulate the PARASOL polarized reflectance,
 418 we use the adding-doubling radiative transfer code for polarized radiative transfer
 419 developed by de Haan et al. (1987).

420 The top panel of Fig. 15 shows the density contours of polarized reflectance
 421 measurements at 865 nm from the PARASOL satellite on 15 October 2007. Over 60,000
 422 ice cloudy pixels over the ocean are included, corresponding to approximately 866,000
 423 total viewing geometries (note that for a given pixel, the PARASOL observations can
 424 provide up to 16 viewing angles). Only the cloudy pixels over the ocean that are

425 determined to be ice phase and with 100% cloud cover are selected (Buriez et al., 1997).
426 Baran and C.-Labonnote (2006) suggested that the peak near scattering angle 142° may
427 be attributed to the influence of water clouds beneath optically thin ice clouds. In the case
428 of a thin ice cloud above a water cloud, the PARASOL cloud mask algorithm may
429 identify the pixel as ice phase although the effect of the underlying water cloud on the
430 observed polarized reflectance is not negligible (Baran and C.-Labonnote, 2006). The
431 middle panel of Fig. 15 shows the differences between the theoretical simulations and
432 observations (i.e., simulations minus observations) assuming smooth ice crystal models.
433 The lower panel of Fig. 15 is similar to the middle panel except the lower panel shows
434 results assuming severely roughened ice crystals. An optimal model should minimize the
435 differences between simulations and observations, thereby leading to the most consistent
436 results. From the comparison between the middle and lower panels, it is clear that the
437 roughened ice crystal model outperforms its smooth counterpart. These results support
438 the conclusion by Zhang et al. (2009) that featureless phase functions should be used for
439 operational satellite data processing.

440

441 **4. Summary**

442

443 This study discusses the development of a library containing the scattering,
444 absorption, and polarization properties of ice particles in the spectral range from $0.2 \mu\text{m}$
445 to $100 \mu\text{m}$. The properties are based on a combination of the Amsterdam discrete dipole
446 approximation (ADDA), the T-matrix method, and the improved geometric-optics
447 method (IGOM). The electromagnetic edge effect is incorporated into the extinction and
448 absorption efficiencies computed from the IGOM. A full set of single-scattering

449 properties is provided by considering three-dimensional random orientations for 11 ice
450 crystal habits: droxtals, prolate spheroids, oblate spheroids, solid and hollow columns,
451 compact aggregates composed of 8 solid columns, hexagonal plates, small spatial
452 aggregates composed of 5 plates, large spatial aggregates composed of 10 plates, and
453 solid and hollow bullet rosettes. The maximum dimension for each habit ranges from 2
454 μm to 10,000 μm at 189 discrete sizes. For each ice habit, three roughness conditions
455 (i.e., smooth, moderately roughened, and severely roughened surfaces) are considered to
456 account for the surface texture for particles having relatively large size parameters. The
457 data library contains the extinction efficiency, single-scattering albedo, asymmetry
458 parameter, six independent non-zero elements of the phase matrix (P_{11} , P_{21} , P_{22} , P_{33} , P_{43} ,
459 and P_{44}), particle projected area, and particle volume.

460 The accuracy of the single-scattering properties for ice particles is improved by taking
461 into consideration each of the following research advancements:

- 462 • Accuracy of the extinction and absorption efficiencies at moderate to large
463 size parameters are improved by the use of an empirical approach to
464 include the edge and the above/below-edge effects on ice crystal optical
465 properties;
- 466 • The single-scattering calculations use an updated compilation of the real
467 and imaginary parts of the refractive index for ice given by Warren and
468 Brandt (2008);
- 469 • The aspect ratio of each habit is consistent for all wavelengths;

- 470 • The phase matrix elements for randomly oriented ice crystals are provided
471 in the database, enabling consideration of the transfer of polarized light
472 beams involving ice clouds;
- 473 • A new treatment of forward scattering in the IGOM is implemented that
474 renders obsolete the delta transmission energy term; and
- 475 • The single-scattering properties are provided for new habits including the
476 hollow bullet rosette and the small and large spatial aggregates of plates.

477 The size of the library is approximately 200 GB, and includes the single-scattering
478 properties of ice crystals covering the wavelengths from UV to far-IR. This data library is
479 complementary to those presented by Kim (2006), Liu (2008), and Hong et al. (2009) for
480 the microwave regime.

481 This library provides the basic single-scattering properties that are critical for ice
482 cloud remote sensing applications and radiative transfer simulations. An illustration of
483 the improved consistency was provided through a comparison of PARASOL polarized
484 reflectance measurements with theoretical simulations. The resulting comparison
485 between measurements and simulations clearly demonstrated that ice cloud optical
486 models assuming severely roughened ice crystals significantly outperform their
487 counterparts assuming smooth ice crystals.

488 Another point made in this study is that the assumption of severe roughening for the
489 ice crystals results in decreasing the asymmetry parameter at solar wavelengths. The
490 decrease of the asymmetry parameter, and use of the featureless phase function, at solar
491 wavelengths implies a decrease in the inferred optical thickness for an ice cloud. This, in

492 turn, will improve the consistency of ice cloud optical thickness inferred from solar and
493 IR wavelengths.

494 In summary, a long-term goal of the authors has been to provide ice crystal single-
495 scattering properties that lead to more consistent retrievals from sensors taking
496 measurements at solar to far-infrared wavelengths, including polarization measurements.
497 This library could be a useful resource for the atmospheric radiative transfer and remote
498 sensing research community.

499 **Acknowledgments**

500 The computation of the present scattering database was mainly supported by a
501 NASA grant (NNX11AK37G) managed by Dr. Lucia Tsaoussi, and partly by the
502 endowment funds related to the David Bullock Harris Chair in Geosciences at the
503 College of Geosciences, Texas A&M University. The long-term effort on the further
504 development and refinement of the Improved Geometric Optics Model (IGOM) was
505 mainly supported by the National Science Foundation (ATM-0239605 and ATM-
506 0803779). Bryan Baum and Ping Yang also gratefully acknowledge the support of the
507 NNX11AR06G managed by Dr. Hal Maring and NNX11AF40G managed by Dr.
508 Ramesh Kakar. George W. Kattawar's research was supported by the Office of Naval
509 Research under contract N00014-11-1-0154. Michael Mishchenko's research was funded
510 by the NASA Remote Sensing Theory Program managed by Dr. Lucia Tsaoussi and the
511 NASA Radiation Sciences Program managed by Dr. Hal Maring. The authors thank M.
512 A. Yurkin and A. G. Hoekstra for the use of their ADDA code (version 0.79), J. F. de
513 Haan for the adding-doubling code for the transfer of polarized radiation, and Y. Xie for
514 the definition of spatial aggregates of hexagonal plates.

515 **References**

- 516 Arnott, W. P., Y. Dong, J. Hallett, and M. R. Poellot, 1994: Role of small ice crystals in
517 radiative properties of cirrus: A case study, FIRE II, November 22, 1991. *J.*
518 *Geophys. Res.*, **99**, 1371– 1381.
- 519 Auer, A. H., Jr., and D. L. Veal, 1970: The dimension of ice crystals in natural clouds. *J.*
520 *Atmos. Sci.*, **27**, 919– 926.
- 521 Baran, A. J., 2009: A review of the light scattering properties of cirrus. *J. Quant.*
522 *Spectrosc. Radiat. Transfer*, **110**, 1239-1598.
- 523 Baran, A. J., and Francis, P. N., 2004: On the radiative properties of cirrus cloud at solar
524 and thermal wavelengths: A test of model consistency using high-resolution
525 airborne radiance measurements, *Q. J. R. Meteorol. Soc.*, **130**, 763--778.
- 526 Baran, A. J. and S. Havemann, 1999: Rapid computation of the optical properties of
527 hexagonal columns using complex angular momentum theory. *J. Quantit.*
528 *Spectrosc. Radiat. Trans.*, **63**, 499--519.
- 529 Baran, A. J., P. Yang, and S. Havemann, 2001: Calculation of the single-scattering
530 properties of randomly oriented hexagonal ice columns: a comparison of the T-
531 matrix and the finite-difference time-domain methods, *Appl. Opt.*, **40**, 4376-4386.
- 532 Baran, A. J., and L. C.-Labonnote, 2006: On the reflection and polarization properties of
533 ice cloud. *J. Quantit. Spectrosc. Radiat. Trans.*, **100**, 41-54.
- 534 Baran, A. J., and L. C.-Labonnote, 2007: A self-consistent scattering model for cirrus. I:
535 The solar region, *Q. J. R. Meteorol. Soc.*, **133**, 1899-1912.

536 Barkey, B., K. N. Liou, Y. Takano, W. Gellerman and P. Sokolsky, 1999: An analog light
537 scattering experiment of hexagonal icelike particles. Part II: Experimental and
538 theoretical results. *J. Atmos. Sci.*, **56**, 613-625.

539 Baum B. A., P. Yang, A. J. Heymsfield, S. Platnick, M. D. King, S. T. Bedka, 2005: Bulk
540 scattering models for the remote sensing of ice clouds. Part 2: Narrowband models. *J.*
541 *Appl. Meteor.*, **44**, 1896-1911.

542 Baum, B. A., P. Yang, Y.-X. Hu , and Q. Feng, 2010: The impact of ice particle
543 roughness on the scattering phase matrix. *J. Quant. Spectrosc. Radiant. Transfer*,
544 Vol. 111, doi:10.1016/j.jqsrt.2010.07.008, 2534-2549.

545 Baum, B. A., P. Yang, A. J. Heymsfield, C. G. Schmitt, Y. Xie, A. Bansemmer, Y.-X. Hu,
546 and Z. Zhang, 2011: Improvements in shortwave bulk scattering and absorption
547 models for the remote sensing of ice clouds. *J. Appl. Meteor. Clim.*, **50**, 1037-
548 1056.

549 Bi, L., P. Yang, G. Kattawar, B. A. Baum, Y. X. Hu, D. M. Winker, R. S. Brock, and J.
550 Q. Lu, 2009: Simulation of the color ratio associated with the backscattering of
551 radiation by ice crystals at 0.532 and 1.064- μm wavelengths. *J. Geophys. Res.*,
552 **114**, D00H08, doi:10.1029/2009JD011759.

553 Bi, L., P. Yang, G. W. Kattawar, and R. Kahn, 2008: Single-scattering properties of tri-
554 axial ellipsoidal particles for a size parameter range from the Rayleigh to
555 geometric-optics regimes. *Appl. Opt.*, **48**, 114-126.

556 Bi, L., P. Yang, G. W. Kattawar, Y. Hu and B. A. Baum, 2011a: Diffraction and external
557 reflection by dielectric faceted particles. *J. Quant. Spectrosc. Radiat Transfer*,
558 **112**, 163-173.

559 Bi, L., P. Yang, G. W. Kattawar, Y. Hu and B. A. Baum, 2011b: Scattering and
560 absorption of light by ice particles: solution by a new physical-geometric optics
561 hybrid method. *J. Quant. Spectrosc. Radiat. Transfer*, **112**, 1492-1508.

562 Bohren, C. F., and D. R. Huffman, 1983: *Absorption and scattering of light by small*
563 *particles*. John Wiley and Sons.

564 Borovoi, A., I. Grishin, E. Naats, and U. Ooppel, 2002: Light backscattering by hexagonal
565 ice crystals. *J. Quant. Spectrosc. Radiat. Transfer*, **72**, 403-417.

566 Buriez, J. C., C. Vanbauce, F. Parol, P. Goloub, M. Herman, B. Bonnel, Y. Fouquart, P.
567 Couvert and G. Seze, 1997: Cloud detection and derivation of cloud properties
568 from POLDER. *Int. J. Remote Sensing*, **18**, 2785-2813

569 Cai, Q. M., and K. N. Liou, 1982: Theory of polarized light scattering by hexagonal ice
570 crystals. *Appl. Opt.*, **21**, 3569-3580.

571 C.-Labonnote, L., G. Brogniez, J. C. Buriez, and M. Doutriaux-Boucher, 2001: Polarized
572 light scattering by inhomogeneous hexagonal monocrystals: Validation with
573 ADEOS-POLDER measurements. *J. Geophys. Res.* , **106**, 12,139-153 .

574 Cole, B. H., P. Yang, B. A. Baum, J. Riedi, L. C.-Labonnote, F. Thieuleux, S. Platnick,
575 2012: Comparison of PARASOL observations with polarized reflectances
576 simulated using different ice habit mixtures, *J. Appl. Meteor. Clim.* (submitted).

577 Connolly, P. J., M. J. Flynn, Z. Ulanowski, T. W. Choullarton, M. W. Gallagher, and K.
578 N. Bower, 2007: Calibration of cloud particle imager probes using calibration
579 beads and ice crystal analogs: the depth of field. *J. Atmos. Oceanic Technol.*, **24**,
580 1860-1879.

581 Cox, S. C. and W. H. Munk, 1954: Measurement of the roughness of the sea surface from
582 photograph's of the sun's glitter. *J. Opt. Soc. Amer.*, **44**, 838 - 850.

583 Davis, P. J., and P. Rabinowitz, 1975: *Methods of Numerical Integration*, Academic
584 Press, 459 pp.

585 de Haan, J. F., P. B. Bosma, and J. W. Hovenier, 1987: The adding method for multiple
586 scattering calculations of polarized light. *Astron. Astrophys.*, **183**, 371-391.

587 Edwards, J. M., S. Havemann, J. C. Thelen, and A. J. Baran, 2007: A new
588 parameterization for the radiative properties of ice crystals: Comparison with
589 existing schemes and impact in a GCM. *Atmos. Res.*, **83**, 19–34.

590 Fu, Q., P. Yang, and W. B. Sun, 1998: An accurate parameterization of the infrared
591 radiative properties of cirrus clouds for climate models. *J. Climate*, **11**, 2223–
592 2237.

593 Gu, Y., J. Farrara, K. N. Liou, and C. R. Mechoso, 2003: Parameterization of cloud-
594 radiation processes in the UCLA general circulation model. *J. Climate*, **16**, 3357-
595 3370.

596 Ham, S.-H., B.-J. Sohn, P. Yang and B. A. Baum, 2009: Assessment of the quality of
597 MODIS cloud products from radiance simulations. *J. Appl. Meteorol. Climatol.*,
598 **48**, 1591-1612.

599 Havemann, S., and A. J. Baran, 2001: Extension of T-matrix to scattering of
600 electromagnetic plane waves by non-axisymmetric dielectric particles: application
601 to hexagonal ice cylinders. *J. Quant. Spectrosc. Radiat. Transfer*, **70**, 139–158.

602 Hess, M. and M. Wiegner, 1994: COP: a data library of optical properties of hexagonal
603 ice crystals. *Appl. Opt.*, **33**, 7740-7746.

604 Hess, M., P. Koepke, and I. Schult, 1998: Optical Properties of Aerosols and Clouds: The
605 Software Package OPAC. *Bull. Am. Met. Soc.*, **79**, 831–844.

606 Hesse, E., and Z. Ulanowski, 2003: Scattering from long prisms computed using ray
607 tracing combined with diffraction on facets. *J. Quant. Spectrosc. Radiat. Transfer*,
608 **79-80**, 721–732.

609 Hong, G., P. Yang, B. A. Baum, A. J. Heymsfield, F. Weng, Q. Liu, G. Heygster, and S.
610 A. Buehler, 2009: Scattering database in the millimeter and submillimeter wave
611 range of 100–1000 GHz for nonspherical ice particles. *J. Geophys. Res.*, **114**,
612 D06201, doi:10.1029/2008JD010451.

613 Huang, H.-L., P. Yang, H. Wei, B.A. Baum, Y. X. Hu, P. Atonelli, and S. A. Ackerman,
614 2004: Inference of ice cloud properties from high-spectral resolution
615 infrared observations. *IEEE Trans. Geosci. Remote Sens.*, **42**, 842-853.

616 Iwabuchi, H., P. Yang, K. N. Liou, and P. Minnis, 2012: Physical and optical properties
617 of persistent contrails: climatology and interpretation, *J. Geophys. Res.*, **117**,
618 D06215, doi:10.1029/2011JD017020.

619 Kahnert, F. M., 2003: Numerical methods in electromagnetic scattering theory. *J. Quant.*
620 *Spectrosc. Radiat. Transfer*, **79–80**, 775–824.

621 Key, J. R., P. Yang, B. A. Baum, and S. L. Nasiri, 2002: Parameterization of shortwave
622 ice cloud optical properties for various particle habits. *J. Geophys. Res.*, **107**,
623 4181, doi:10.1029/2001JD000742.

624 Kim, M.-J., 2006 : Single scattering parameters of randomly oriented snow particles at
625 microwave frequencies. *J. Geophys. Res.*, **111**, D14201,
626 doi:10.1029/2005JD006892.

627 King, M. D., S. Platnick, P. Yang, G. T. Arnold, M. A. Gray, J. C. Riedi, S. A.
628 Ackerman, and K. N. Liou, 2004: Remote sensing of liquid water and ice cloud
629 optical thickness, and effective radius in the Arctic: Application of air-borne
630 multispectral MAS data. *J. Atmos. and Ocean. Technol.*, **21**, 857-875.

631 Liou, K. N., 1986: Influence of cirrus clouds on weather and climate processes: A
632 global perspective. *Mon. Wea. Rev.*, **114**, 1167-1199.

633 Liou, K. N., 2002: *An Introduction to Atmospheric Radiation*. 2nd edition, Academic
634 Press, San Diego.

635 Liou, K. N., Y. Gu, Q. Yue, and G. McFarguhar, 2008: On the correlation between ice
636 water content and ice crystal size and its application to radiative transfer and
637 general circulation models. *Geophys. Res. Lett.*, **35**, L13805,
638 doi:10.1029/2008GL033918.

639 Liou, K. N., Y. Takano, and P. Yang, 2010: On geometric optics and surface waves for
640 light scattering by spheres. *J. Quant. Spectrosc. Radiat. Transfer*, **111**, 1980–
641 1989, doi:10.1016/j.jqsrt.2010.04.004.

642 Liou, K. N., Y. Takano, and P. Yang, 2011: Light absorption and scattering by
643 aggregates: Application to black carbon and snow grain. *J. Quant. Spectrosc.*
644 *Radiat. Transfer*, **112**, 1581–1594, doi:10.1016/j.jqsrt.2011.03.007.

645 Liu, G., 2008 : A database of microwave single-scattering properties for nonspherical ice
646 particles. *Bull. Amer. Meteor. Soc.*, **89**, 1563-1570.

647 Lynch, D. K., K. Sassen. D. O. Starr, and G. Stephens, 2002: *Cirrus*. Oxford University
648 Press, 480 pp.

649 Macke, A., 1993: Scattering of light by polyhedral ice crystals. *Appl. Opt.*, **32**, 2780–
650 2788.

651 Macke, A., J. Mueller, and E. Raschke, 1996a: Single scattering properties of
652 atmospheric ice crystal. *J. Atmos. Sci.*, **53**, 2813-2825.

653 Macke, A., M. I. Mishchenko, and B. Cains, 1996b: The influence of inclusions on light
654 scattering by large ice particles, *J. Geophys. Res.*, **101**, 23,311-23,316.

655 Mayer B., and A. Kylling, 2005: Technical Note: The libRadtran software package for
656 radiative transfer calculations: Description and examples of use. *Atmos. Chem.*
657 *Phys.*, **5**, 1855-1877.

658 McFarquhar, G. M., P. Yang, A. Macke, and A. J. Baran, 2002: A new parameterization
659 of single-scattering solar radiative properties for tropical anvils using observed ice
660 crystal size and shape distributions. *J. Atmos. Sci.*, **59**, 2458-2478.

661 Minnis, P., S. Sun-Mack, D. F. Young, P. W. Heck, D. P. Garber, Y. Chen, D. A.
662 Spangenberg, R. F. Arduini, Q. Z. Trepte, W. L. Smith, Jr., J. K. Ayers, S. C.
663 Gibson, W. F. Miller, V. Chakrapani, Y. Takano, K. N. Liou, Y. Xie and P. Yang,
664 2011: CERES edition-2 cloud property retrievals using TRMM VIRS and
665 TERRA and AQUA MODIS data -- part I: Algorithms. *IEEE Trans. Geosci.*
666 *Remote Sens.*, **49**, 4374-4400.

667 Mishchenko, M. I., and A. Macke, 1998: Incorporation of physical optics effects and
668 computations of the Legendre expansion for ray-tracing phase functions involving
669 delta-function transmission, *J. Geophys. Res.*, **103**, 1799-1805.

670 Mishchenko, M. I., and K. Sassen, 1998: Depolarization of lidar returns by small ice
671 crystals: An application to contrails, *Geophys. Res. Lett.*, **25**(3), 309-312.

672 Mishchenko, M. I., L. D. Travis, and D. W. Mackowski, 1996: T-matrix computations of
673 light scattering by nonspherical particles: A review. *J. Quant. Spectrosc. Radiat.*
674 *Transfer*, **55**, 535-575.

675 Mishchenko, M. I., L. D. Travis, and A. A. Lacis, 2002: *Scattering, Absorption, and*
676 *Emission of Light by Small Particles*, Cambridge University Press, Cambridge.

677 Mishchenko, M. I., W. J. Wiscombe, J. W. Hovenier, and L. D. Travis, 2000: Overview
678 of scattering by nonspherical particles, *Light Scattering by Nonspherical*
679 *Particles: Theory, Measurements, and Geophysical Applications*, M. I.
680 Mishchenko, J. W. Hovenier, and L. D. Travis (eds), pp. 29-60, Academic Press,
681 San Diego, CA.

682 Mitchell, D. L., and W. P. Arnott, 1994: A model predicting the evolution of ice
683 particle size spectra and radiative properties of cirrus clouds: Part II.
684 Dependence of absorption and extinction on ice crystal morphology. *J.*
685 *Atmos. Sci.*, **51**, 817– 832.

686 Muinonen, K., 1989: Scattering of light by crystals: a modified Kirchhoff approximation.
687 *Appl. Opt.*, **28**, 3044-3050.

688 Nakajima, T. Y., Teruyuki Nakajima, Kyu Yoshimori, Sumit K. Mishra, and Sachchida
689 N. Tripathi, 2009: Development of a light scattering solver applicable to particles
690 of arbitrary shape on the basis of the surface-integral equations method of Müller
691 type. I. Methodology, accuracy of calculation, and electromagnetic current on the
692 particle surface. *Appl. Opt.*, **48**, 3526-3536.

693 Nussenzveig, H. M., and W. J. Wiscombe, 1980: Efficiency factors in Mie Scattering.
694 *Physical Review Letter*, **18**, 1490–1494.

695 Platnick, S., M. D. King, S. A. Ackerman, W. P. Menzel, B. A. Baum, J. C. Riedi, and R.
696 A. Frey, 2003: The MODIS cloud products: Algorithms and examples from Terra.
697 *IEEE Trans. Geosci. Remote Sens.*, **41**, 459–473.

698 Pruppacher, H. R., and J. D. Klett, 1980: *Microphysics of Clouds and Precipitation*.
699 Springer, 714 pp.

700 Schmitt, C. G., and A. J. Heymsfield, 2007: On the occurrence of hollow bullet rosette
701 and column shaped ice crystals in midlatitude cirrus. *J. Atmos. Sci.*, **64**, 4515–
702 4520.

703 Sun, W., Q. Fu, and Z. Chen, 1999: Finite-difference time-domain solution of light
704 scattering by dielectric particles with perfectly matched layer absorbing boundary
705 conditions. *Appl. Opt.*, **38**, 3141–3151.

706 Takano, Y, and K. N. Liou, 1989 : Solar radiative transfer in cirrus clouds. Part I. Single-
707 scattering and optical properties of hexagonal ice crystals. *J. Atmos. Sci.*, **46**, 3-19.

708 Takano, Y. and K. N. Liou, 1995: Radiative transfer in cirrus clouds. III. Light scattering
709 by irregular ice crystals. *J. Atmos. Sci.*, **52**, 818-837.

710 Ulanowski, Z., E. Hesse, P. H. Kaye, and A. J. Baran, 2006, Light scattering by complex
711 ice-analogue crystals. *Journal of Quantitative Spectroscopy and Radiative*
712 *Transfer*, **100**, 382-392.

713 Um, J.S., and G. M. McFarquhar, 2007: Single-scattering properties of aggregates of
714 bullet rosettes in cirrus. *J. Appl. Meteor. Climat.*, **46**, 757-775.

715 van de Hulst, H. C., 1957: *Light Scattering by Small Particles*. Dover, 470 pp.

716 Walden, V. P., S. G. Warren, and E. Tuttle, 2003: Atmospheric ice crystals over the
717 Antarctic Plateau in winter. *J. Appl. Meteor.*, **42**, 1391–1405.

718 Wang, X., K. N. Liou, S. C. Ou, G. G. Mace, and M. Deng, 2009: Remote sensing of
719 cirrus cloud vertical size profile using MODIS data. *J. Geophys. Res.*, **114**,
720 D09205, doi:10.1029/2008JD011327.

721 Warren, S. G., and R. E. Brandt, 2008: Optical constants of ice from the ultraviolet to the
722 microwave: A revised compilation. *J. Geophys. Res.*, **113**, D14220,
723 doi:10.1029/2007JD009744.

724 Wendisch, M., P. Yang, and P. Pilewskie, 2007: Effects of ice crystal habit on the
725 thermal infrared radiative properties and forcing of cirrus clouds. *J. Geophys.*
726 *Res.*, **112**, D08201, doi:10.1029/2006JD007899.

727 Wendling, P., R. Wendling, and H. K. Weickmann, 1979: Scattering of solar radiation by
728 hexagonal ice crystals. *Appl. Opt.*, **18**, 2663–2671.

729 Westbrook, C. D., R. C. Ball, P. R. Field, and A. J. Heymsfield, 2004, Theory of growth
730 by differential sedimentation, with application to snowflake formation. *Phys. Rev.*
731 *E*, **70**, Art. No. 021403.

732 Wriedt, T. 2009: Light scattering theories and computer codes. *J. Quant. Spectrosc.*
733 *Radiat. Transfer*, **110**, 833–843.

734 Xie, Y., P. Yang, G. W. Kattawar, B. A. Baum and Y. Hu, 2011: Simulation of the
735 optical properties of plate aggregates for application to the remote sensing of
736 cirrus clouds, *Appl. Opt.*, **50**, 1065-1081.

737 Yang, P, G. Hong, A. E. Dessler, S. C. Ou, K. N. Liou, P. Minnis, and Hashvardhan,
738 2010: Contrails and Induced Cirrus: Optics and Radiation, *Bull. Am. Met. Soc.*, **91**,
739 473-478.

740 Yang, P., and K. N. Liou, 1996a: Finite-difference time domain method for light scat-
741 tering by small ice crystals in three-dimensional space. *J. Opt. Soc. Amer. A*, **13**,
742 2072–2085.

743 Yang, P., and K. N. Liou, 1996b: Geometric-optics-integral-equation method for light
744 scattering by nonspherical ice crystals. *Appl. Opt.*, **35**, 6568–6584.

745 Yang, P., and K. N. Liou, 1998: Single-scattering properties of complex ice crystals in
746 terrestrial atmosphere. *Contr. Atmos. Phys.*, **71**, 223-248.

747 Yang, P., and K. N. Liou, 2009a: Effective refractive index for determining ray
748 propagation in an absorbing dielectric particle. *J. Quant. Spectrosc. Radiat.*
749 *Transfer.*, **110**, 300-306.

750 Yang, P., and K. N. Liou, 2009b: An “exact” geometric-optics approach for computing
751 the optical properties of large absorbing particles. *J. Quant. Spectrosc. Radiat.*
752 *Transfer.*, **110**, 1162-1177.

753 Yang, P., B. A. Baum, A. J. Heymsfield, Y. X. Hu, H.-L. Huang, S.-C. Tsay, and S.
754 Ackerman, 2003: Single-scattering properties of droxtals. *J. Quant. Spectrosc.*
755 *Radiat. Transfer*, **79-80**, 1159– 1169.

756 Yang, P., H. Wei, H.-L. Huang, B. A. Baum, Y. X. Hu, G. W. Kattawar, M. I.
757 Mishchenko, and Q. Fu, 2005: Scattering and absorption property database for
758 nonspherical ice particles in the near- through far-infrared spectral region. *Appl.*
759 *Opt.*, **44**, 5512-5523.

760 Yang, P., K. N. Liou, K. Wyser, and D. Mitchell, 2000: Parameterization of the scattering
761 and absorption properties of individual ice crystals. *J. Geophys. Res.*, **105**, 4699-
762 4718.

763 Yang, P., Z. Zhang, G. W. Kattawar, S. G. Warren, B. A. Baum, H.-L. Huang, Y. Hu, D.
764 Winker, and J. Iaquina, 2008a: Effect of cavities on the optical properties of
765 bullet rosettes: Implications for active and passive remote sensing of ice
766 cloud properties. *J. Appl. Meteor. Clim.*, **47**, 2311-2330.

767 Yang, P., G. Hong, G. W. Kattawar, P. Minnis and Y. Hu, 2008b: Uncertainties
768 associated with the surface texture of ice particles in satellite-based retrieval
769 of cirrus clouds: Part II. Effect of particle surface roughness on retrieved
770 cloud optical thickness and effective particle size, *IEEE Transactions on*
771 *Geosciences and Remote Sensing*, **46**, 1948-1957.

772 Yee, S. K., 1966: Numerical solution of initial boundary value problems involving
773 Maxwell's equations in isotropic media. *IEEE Trans. Antennas Propagat.*, **14**,
774 302–307.

775 Yue, Q., K. N. Liou, S. C. Ou, B. H. Kahn, P. Yang, and G. G. Mace, 2007:
776 Interpretation of AIRS data in thin cirrus atmospheres based on a fast radiative
777 transfer model. *J. Atmos. Sci.*, **64**, 3827 - 3842.

778 Yurkin, M. A., V. P. Maltsev, A. G. Hoekstra, 2007a: The discrete dipole approximation
779 for simulation of light scattering by particles much larger than the wavelength. *J*
780 *Quant Spectrosc Radiat Transfer*, **106**, 546–557.

781 Yurkin, M.A., A.G. Hoekstra, R. Scott Brock and J.Q. Lu, 2007b : Systematic
782 comparison of the discrete dipole approximation and the finite difference time
783 domain method for large dielectric scatterers. *Optics Express*, **15**, 17902–17911.

784 Zhang, Z., P. Yang, G. W. Kattawar, J. Riedi, L. C.-Labonnote, B. A. Baum, S. Platnick,
785 and H.-L. Huang, 2009: Influence of ice particle model on retrieving cloud

786 optical thickness from satellite measurements: model comparison and
787 implication for climate study. *Atmos. Chem. Phys.*, **9**, 7115-7129.

788 Zhang, Z., P. Yang, G. W. Kattawar, S.-C. Tsay, B. A. Baum, H.-L. Huang, Y. X. Hu, A. J.
789 Heymsfield, and J. Reichardt, 2004: Geometric optics solution to light
790 scattering by droxtal ice crystals. *Appl. Opt.*, **43**, 2490–2499.

791

792 **Figure Captions:**

793

794 Table 1. Geometric parameters of ice crystal habits.

795

796

797 Fig. 1. (a) Correlation of the real and imaginary part of the refractive index. (b) Real part
798 of the refractive index. (c) Imaginary part of the refractive index.

799

800 Fig. 2. Grid points in the computational domain of the particle size and the wavelength.

801 The left panel is for the previous databases, and the right panel is for the present database.

802

803 Fig. 3. Ice crystal habits: quasi-spherical, column-type, plate-type, and bullet rosette
804 particles.

805

806 Fig. 4. Comparison of the phase matrix elements from the FDTD and the ADDA at the
807 wavelengths of 0.66 μm and 12 μm .

808

809 Fig. 5. Number of ADDA simulations (or particle orientations specified by β and γ) at
810 four representative wavelengths in the hexagonal columns case.

811

812 Fig. 6. Ray types: (a) edge rays, (b) grazing rays, and (c) rays incident on the particle.

813

814 Fig.7. Edge/tunneling effect contribution to the extinction efficiency, the absorption
815 efficiency, and the single-scattering albedo.

816

817 Fig. 8. Spectral variation of the extinction, the single-scattering albedo, and the
818 asymmetry factor at the particle maximum dimension of 15 μm .

819

820 Fig. 9. Similar to Fig. 8, but for the particle maximum dimension of 200 μm .

821

822 Fig. 10. Contours of the extinction efficiency, the single-scattering albedo, and the
823 asymmetry factor for an aggregate of 10 plates (left) and a hollow bullet rosette (right).

824

825 Fig. 11. Comparison of the phase matrix elements for an aggregate of 10 plates and a
826 hollow bullet rosette at the size of 20 μm .

827

828 Fig. 12. Similar to Fig. 11, except the size is 2000 μm .

829

830 Fig. 13. Comparison of the phase function and the asymmetry factor for smooth (solid
831 lines) and roughened (dashed lines) ice crystals.

832

833 Fig. 14. Upper panel: ice crystal habit distribution assumed for MODIS Collection 5 ice
834 cloud property retrieval. Middle panel: comparison of the phase functions of smooth and
835 roughened ice crystals with an effective particle size of 50 μm based on the habit
836 distribution in the upper panel, and the phase matrix element ratio $-P_{12}/P_{11}$
837 corresponding to the phase functions in the middle panel.

838

839 Fig. 15. Upper panel: density contours of polarized reflectance measurements at 865 nm
840 from the PARASOL satellite on 15 October 2007. Over 60,000 pixels over the ocean are

841 included, corresponding to approximately 866,000 total viewing geometries plotted.
842 Middle panel: the difference between simulated polarized reflectance and measured
843 polarized reflectance for each viewing geometry. The MODIS collection 5 habit
844 distribution and smooth ice particles with an effective diameter of 50 μm were used in the
845 simulation, and the optical depth was 5. Lower panel: the difference in polarized
846 reflectance using C5 with severely roughened ice particles and all simulation parameters
847 the same as the middle panel.

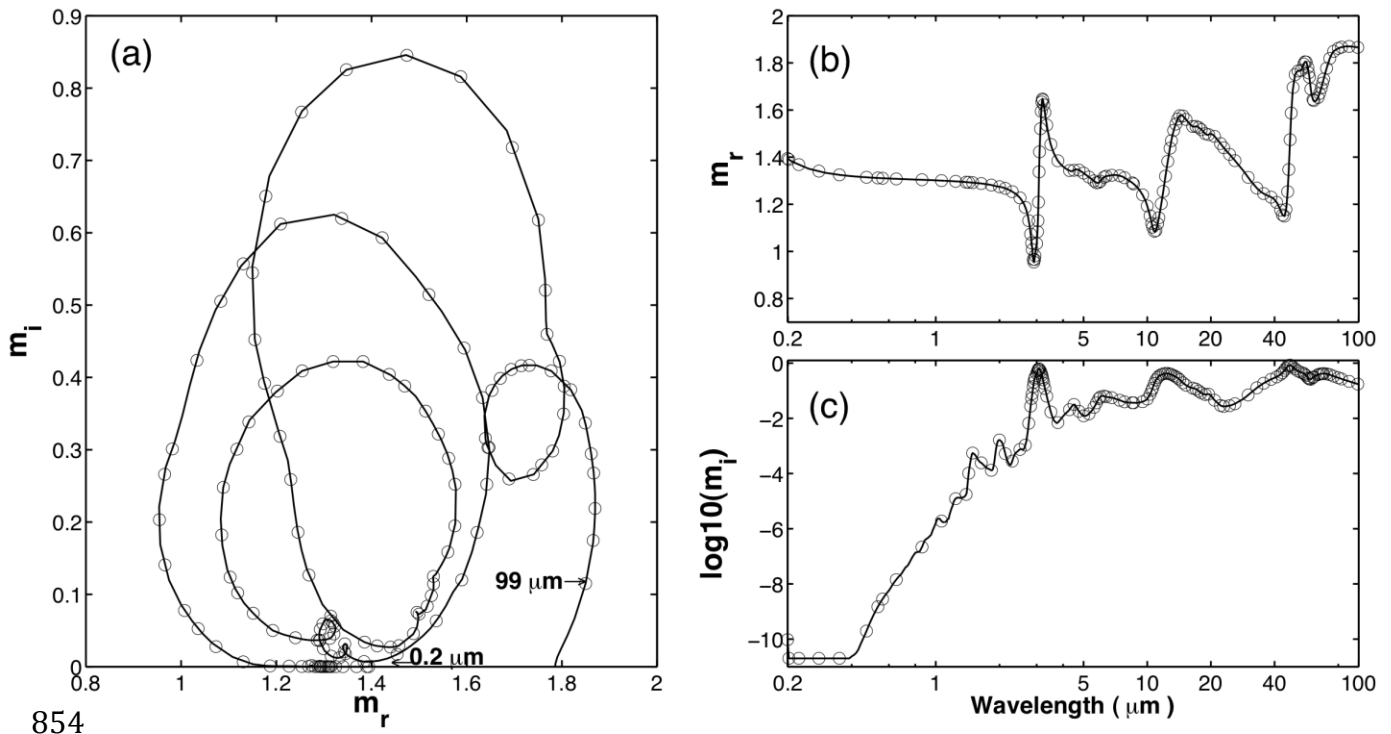
848
849

850 Table 1. Geometric parameters of ice crystal habits.
851

Droxtal	$\theta_1 = 32.35^\circ, \theta_2 = 71.81^\circ$								
Prolate spheroids	$a/c = 0.725, 0.5, 0.25$								
Oblate spheroids	$a/c = 1.25, 2.5, 4$								
Column	$2a/L = \begin{cases} 0.7, & L < 100 \mu m \\ 6.96/\sqrt{L}, & L \geq 100 \mu m \end{cases}$								
Hollow column	$2a/L = \begin{cases} 0.7, & L < 100 \mu m \\ 6.96/\sqrt{L}, & L \geq 100 \mu m \end{cases}, d = 0.25L$								
Aggregate of 8 columns	#	a	L	α	β	γ	X0	Y0	Z0
	1	46	158	23	50	-54	0	0	0
	2	40	124	16	81	156	15.808	105.189	-60.108
	3	28	78	5	57	94	-26.691	73.005	47.369
	4	48	126	13	76	130	-85.688	-39.19	-11.643
	5	53	144	11	29	-21	104.532	33.08	27.801
	6	19	54	8	62	-164	35.923	-49.692	-37.533
	7	34	102	29	41	60	40.11	-57.227	110.238
	8	43	138	19	23	-122	-9.7524	-129.313	57.131
Plate	$2a/L = \begin{cases} 1, & a \leq 2\mu m \\ 0.2914a + 0.4172, & 2\mu m < a < 5\mu m \\ 0.8038a^{0.526}, & a \geq 5\mu m \end{cases}$								
Aggregate of 5 plates	#	a	L	α	β	γ	X0	Y0	Z0
	1	24	11.223	0	0	0	0	0	0
	2	27	11.868	-82.655	175.767	-78.103	-5.664	43.934	-13.203
	3	22	10.770	-7.651	-23.688	-132.443	-13.519	21.792	-25.347
	4	20	10.294	-101.85	155.069	-50.708	18.656	68.178	-29.741
	5	38	13.955	-118.412	-30.374	-42.438	-3.161	71.109	-54.738
Aggregate of 10 plates	#	a	L	α	β	γ	X0	Y0	Z0
	1	77	19.503	0	0	0	0	0	0
	2	58	17.052	-177.37	64.830	-27.941	99.193	4.561	-7.3748
	3	75	19.261	-146.82	242.688	-69.303	115.667	8.322	-105.096
	4	42	14.633	99.056	53.002	77.723	90.671	21.580	-175.875
	5	47	15.434	13.853	224.545	33.875	-18.069	47.826	47.2620
	6	72	18.892	-167.855	43.472	-23.762	97.754	-22.864	-249.469
	7	45	15.119	-108.623	217.569	-15.595	7.019	-35.116	-189.123
	8	65	17.998	-51.308	-72.4	-173.509	-14.105	-132.186	-184.875
	9	74	19.139	-87.353	75.060	-49.382	32.361	-171.149	-155.846
	10	70	18.6414	-98.0649	-111.24	25.5653	50.0817	-228.132	-81.978
Solid bullet rosettes	$2a/L = 2.3104L^{-0.37}, t = (\sqrt{3}/2)a/\tan(28^\circ)$								
Hollow bullet rosettes	$2a/L = 2.3104L^{-0.37}, t = (\sqrt{3}/2)a/\tan(28^\circ), H = 0.5(t + L)$								

852

853

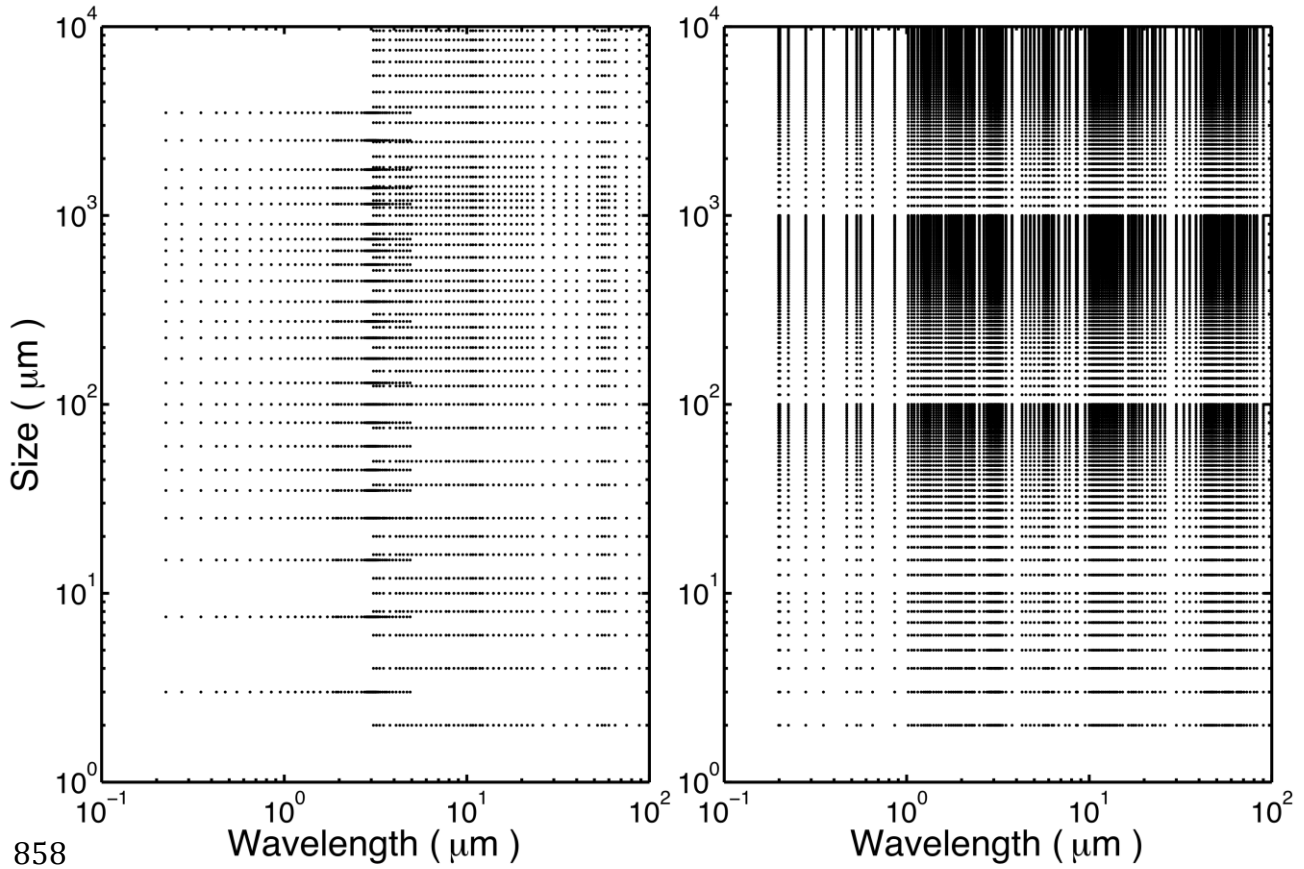


854

855 Fig. 1. (a) Correlation of the real and imaginary part of the refractive index. (b) Real part

856 of the refractive index. (c) Imaginary part of the refractive index.

857



858

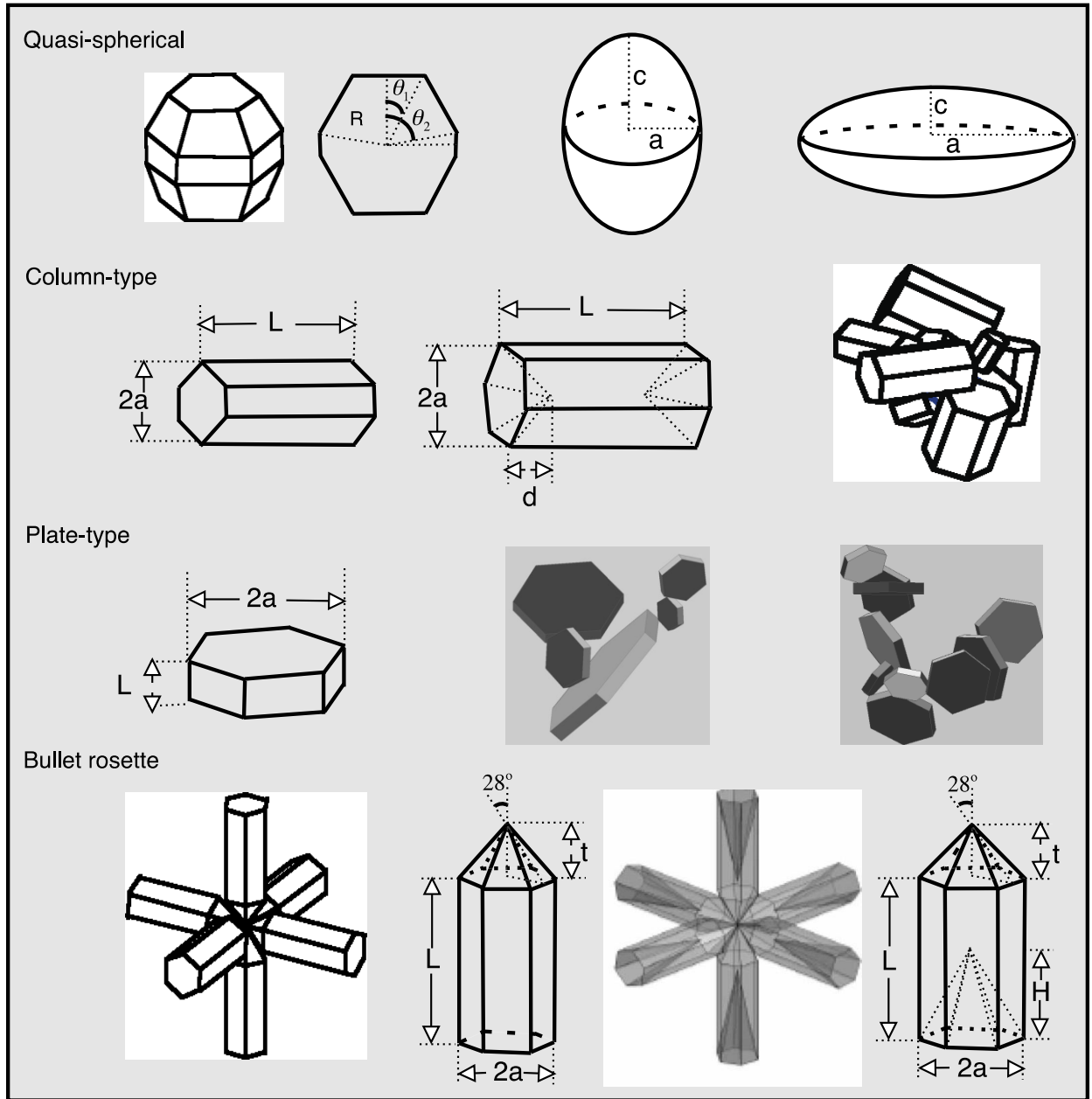
859

860 Fig. 2. Grid points in the computational domain of the particle size and the wavelength.

861 The left panel is for the previous databases, and the right panel is for the present database.

862

863



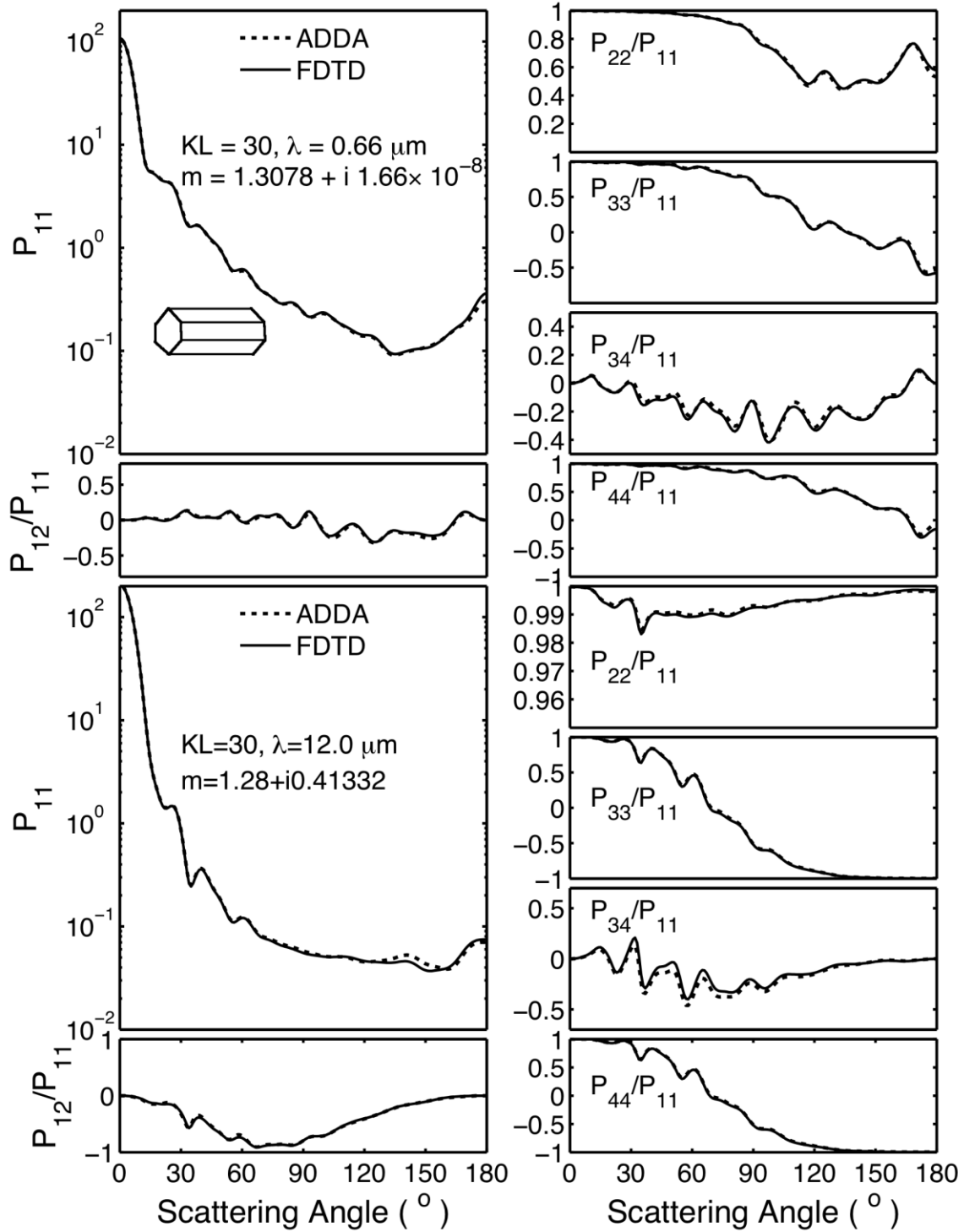
864

865

866 Fig. 3. Ice crystal habits: quasi-spherical, column-type, plate-type, and bullet rosette

867 particles.

868

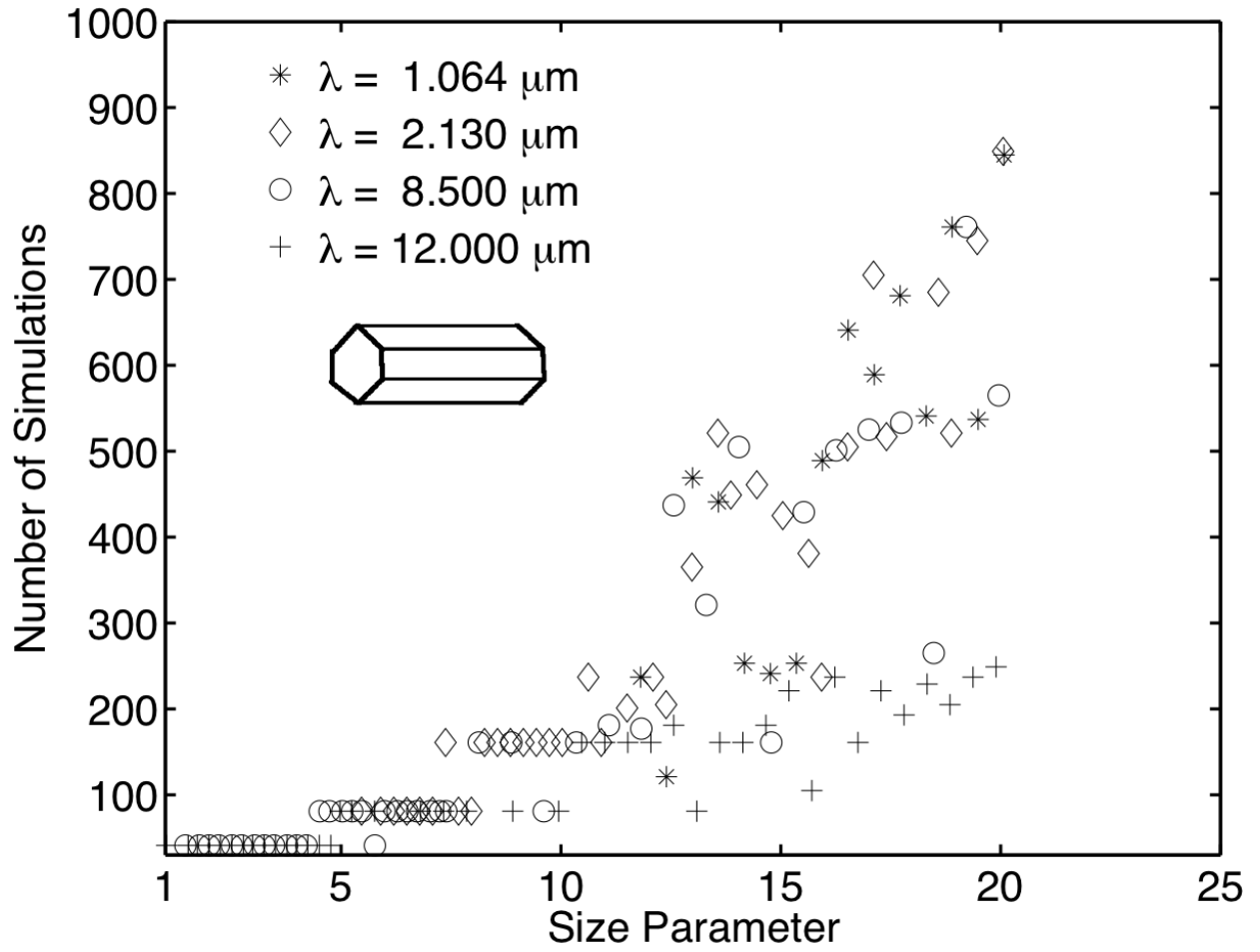


869

870 Fig. 4. Comparison of the phase matrix elements from the FDTD and the ADDA at the

871 wavelengths of 0.66 μm and 12 μm.

872



873

874

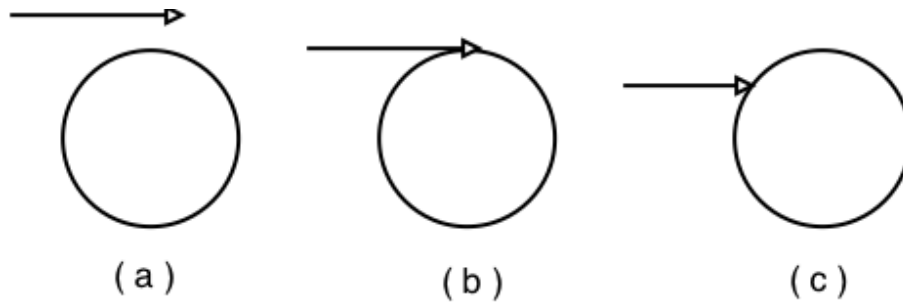
875 Fig. 5. Number of ADDA simulations (or particle orientations specified by β and γ) at

876 four representative wavelengths in the hexagonal columns case.

877

878

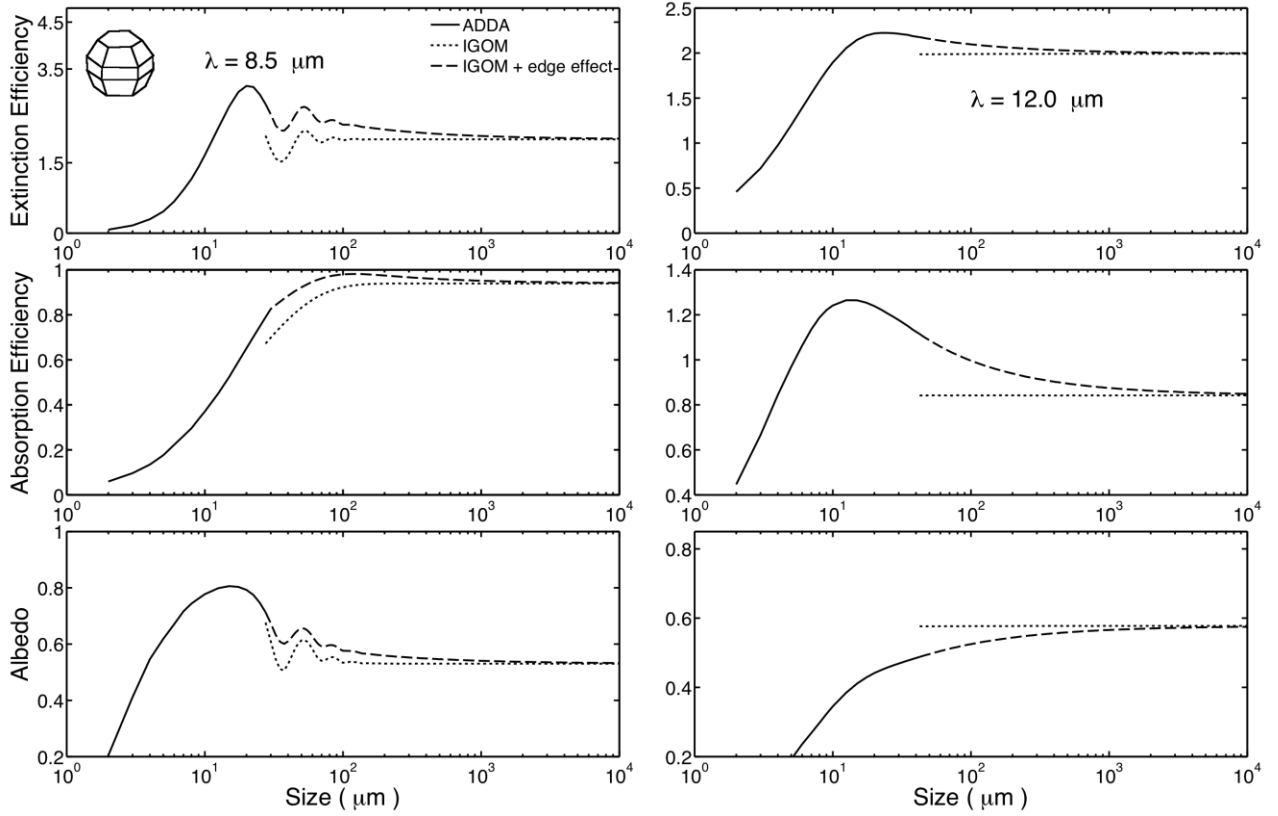
879



880

881 Fig. 6. Ray types: (a) edge rays, (b) grazing rays, and (c) rays incident on the particle.

882

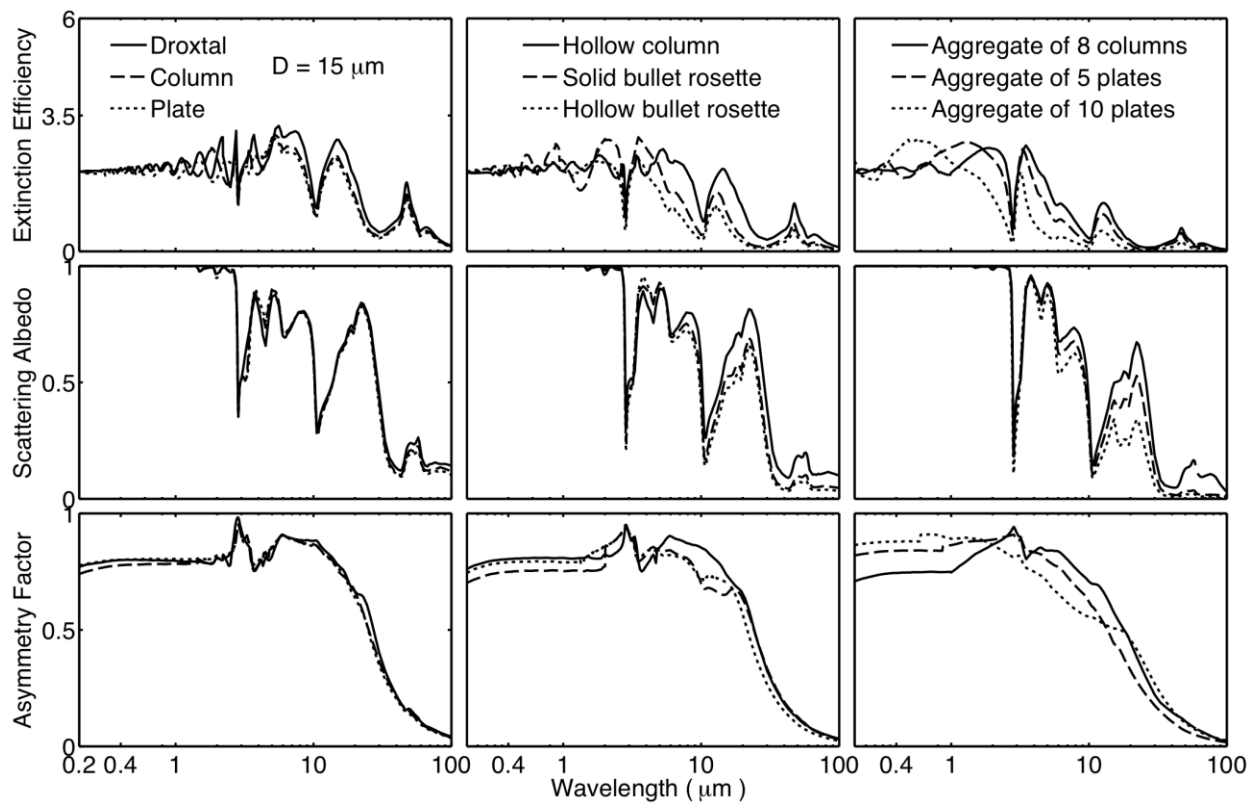


883

884

885 Fig.7. Edge/tunneling effect contribution to the extinction efficiency, the absorption

886 efficiency, and the single-scattering albedo.

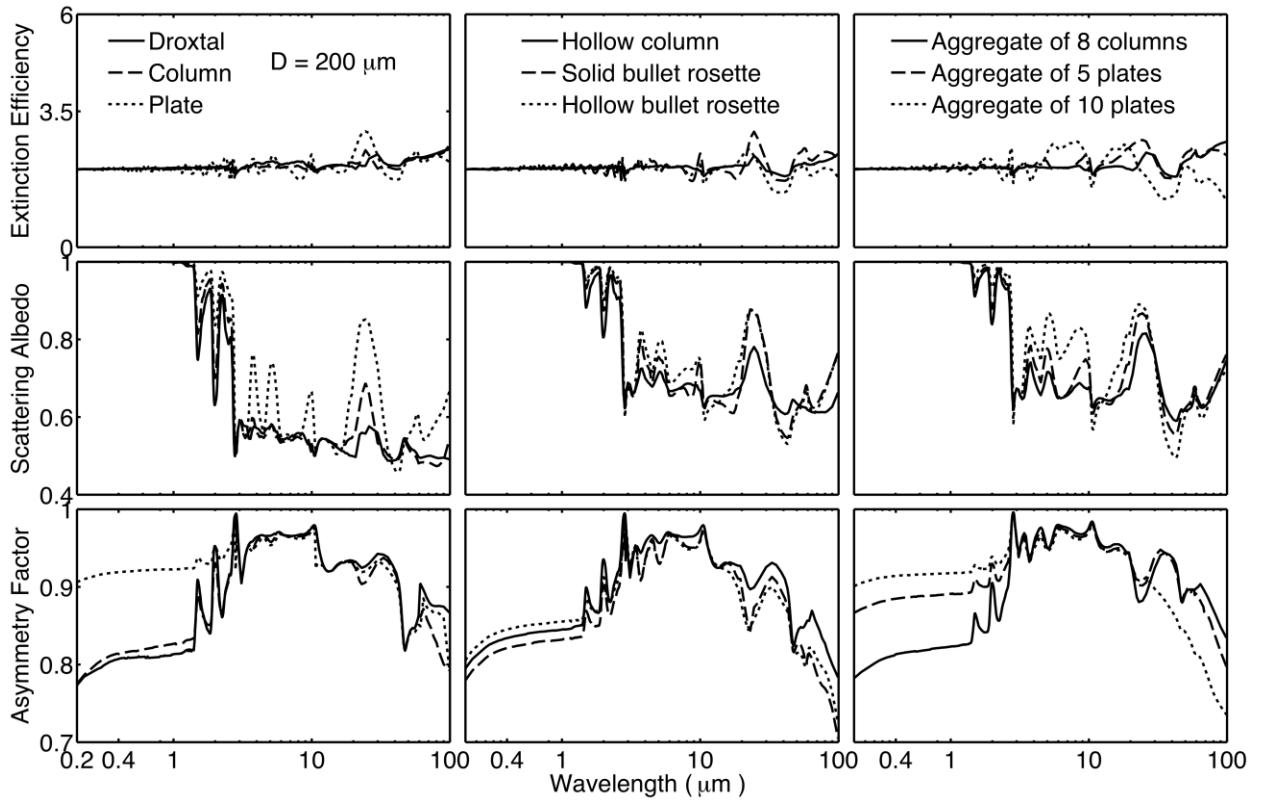


887

888

889 Fig. 8. Spectral variation of the extinction, the single-scattering albedo, and the
 890 asymmetry factor at the particle maximum dimension of $15 \mu\text{m}$.

891

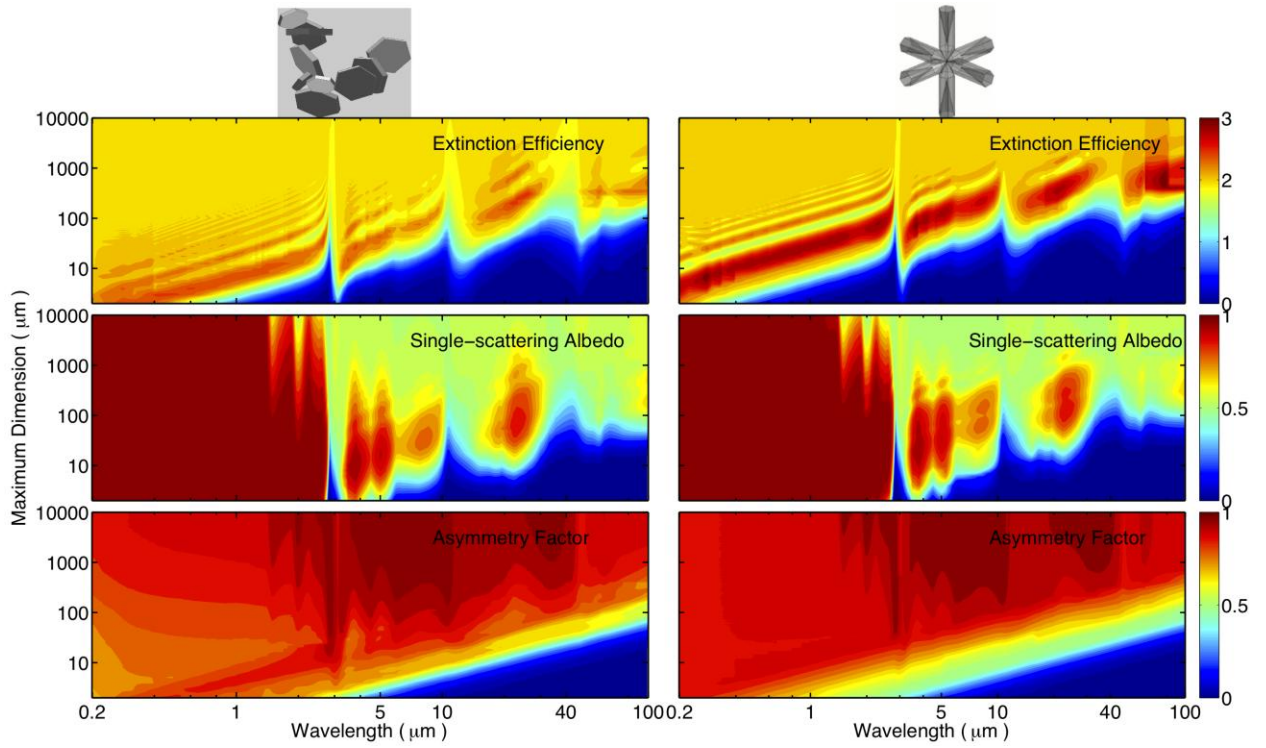


892

893

894 Fig. 9. Similar to Fig. 8, but for the particle maximum dimension of $200 \mu\text{m}$.

895



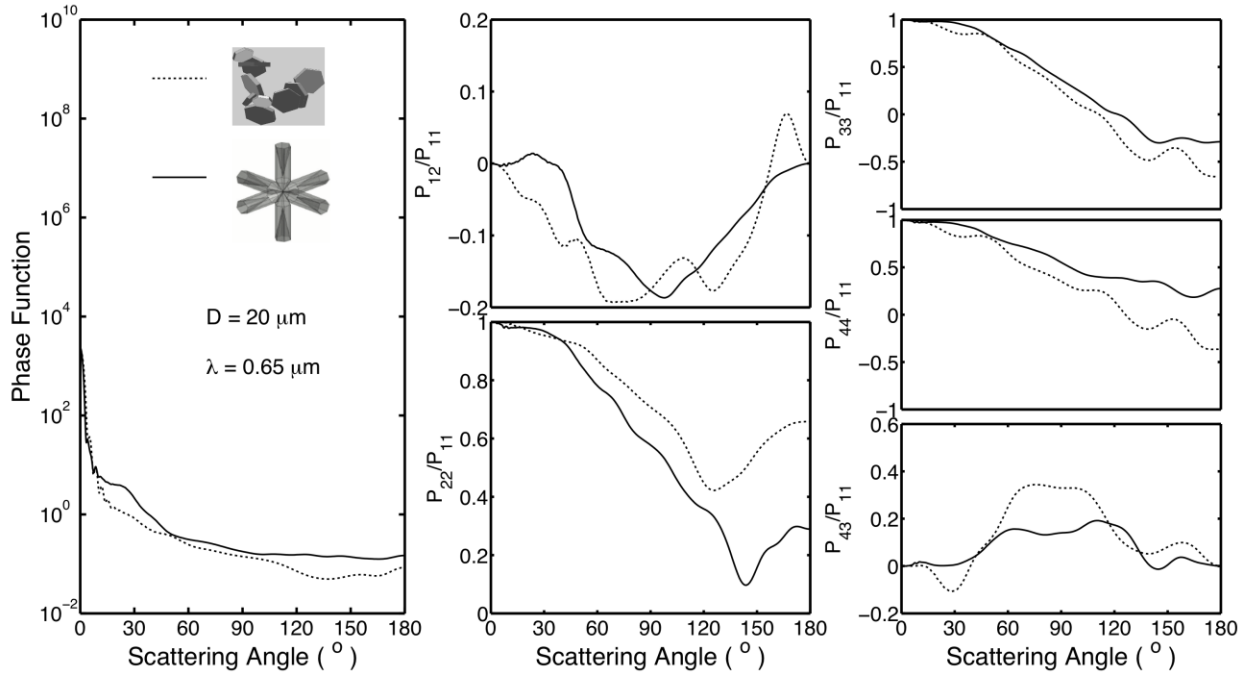
896

897

898 Fig. 10. Contours of the extinction efficiency, the single-scattering albedo, and the
 899 asymmetry factor for an aggregate of 10 plates (left) and a hollow bullet rosette (right).

900

901



902

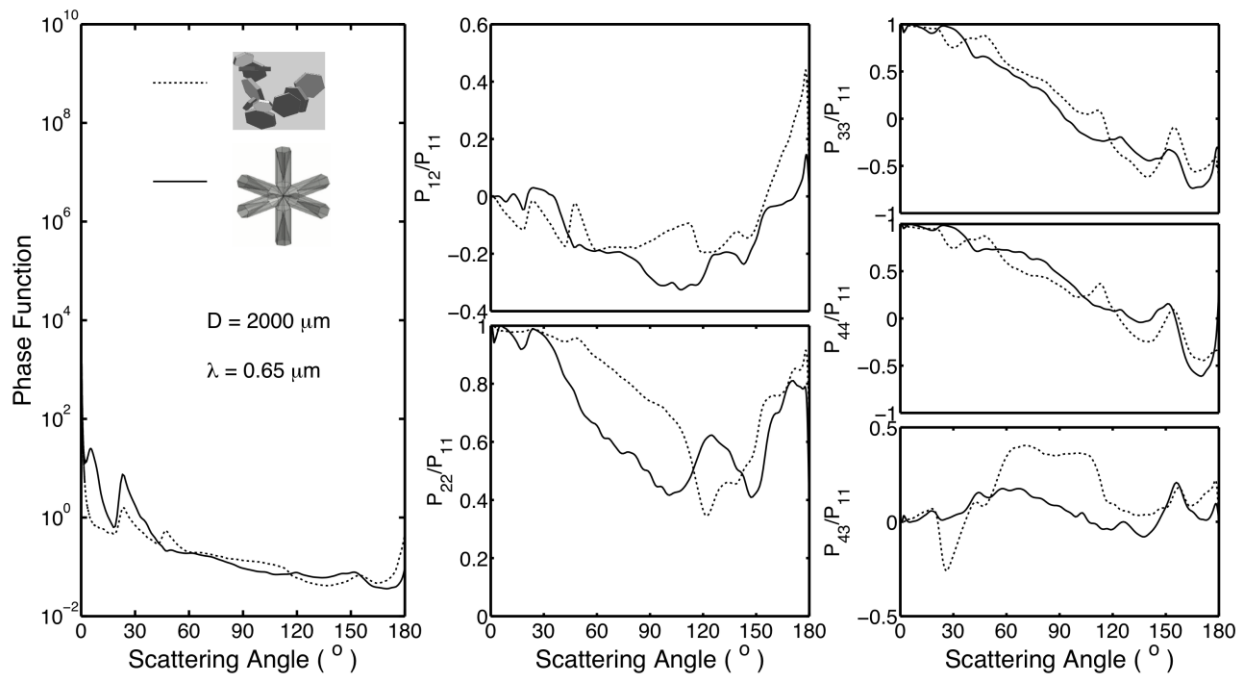
903

904 Fig. 11. Comparison of the phase matrix elements for an aggregate of 10 plates and a
905 hollow bullet rosette at the size of 20 μm .

906

907

908

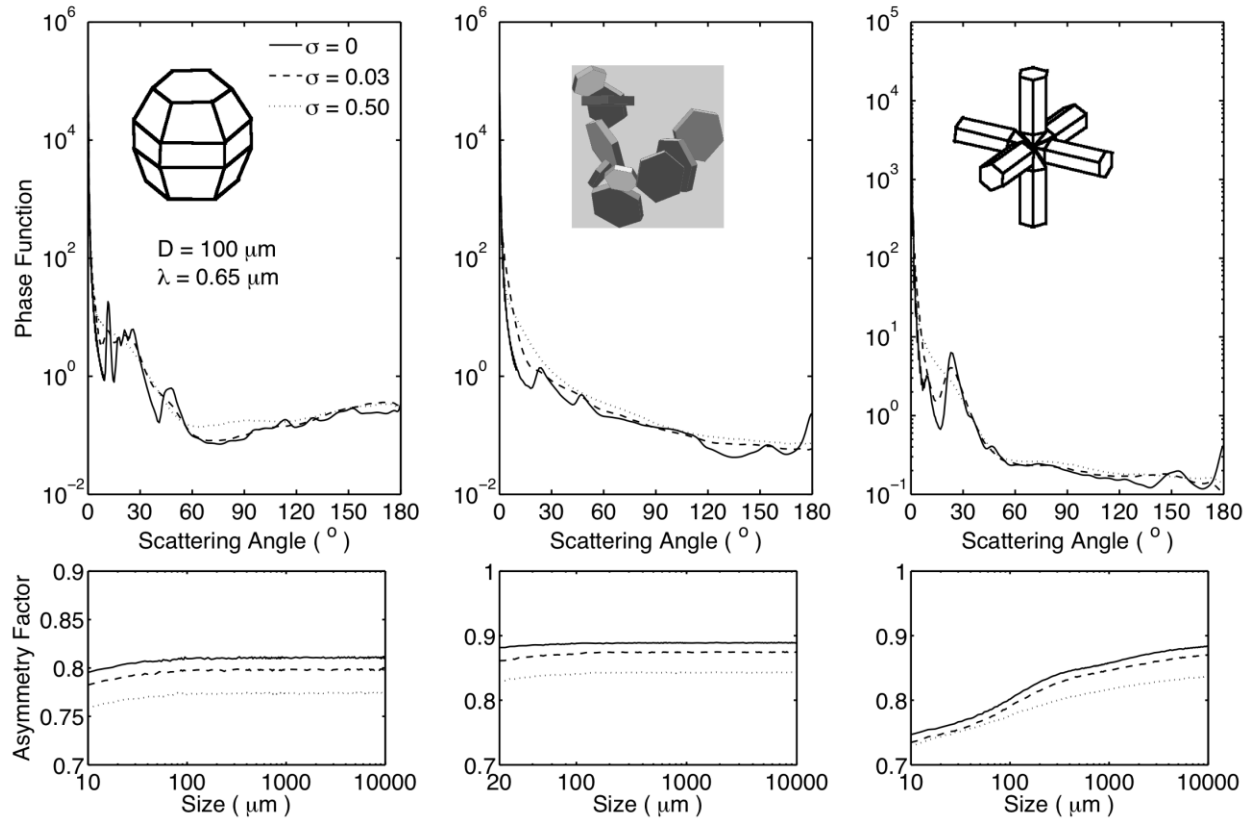


909

910

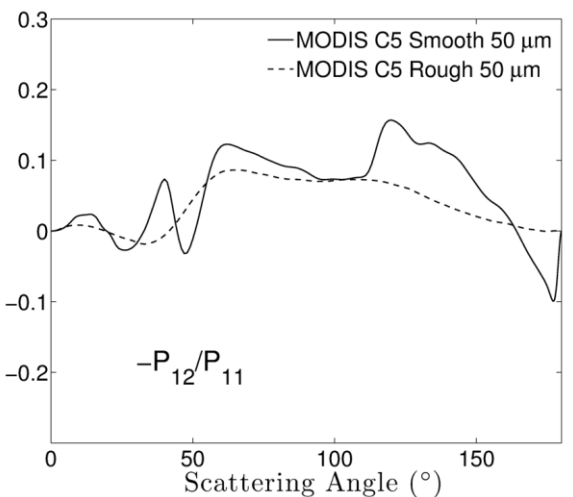
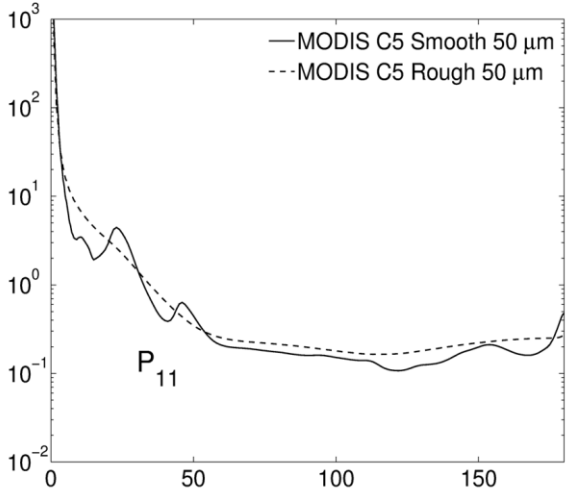
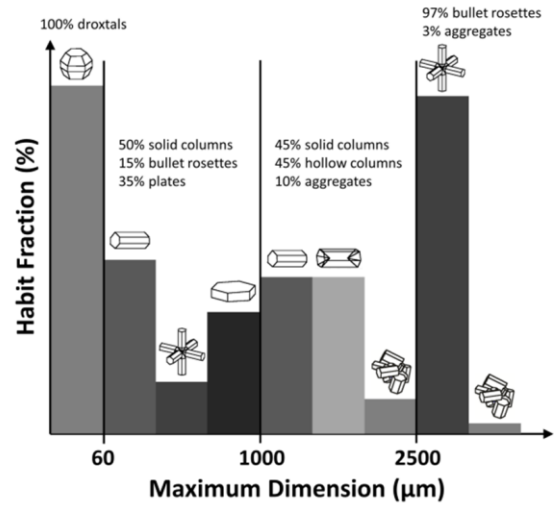
911 Fig. 12. Similar to Fig. 11, except the size is $2000 \mu\text{m}$.

912



913
 914
 915
 916
 917

Fig. 13. Comparison of the phase function and the asymmetry factor for smooth (solid lines) and roughened (dashed lines) ice crystals.



918
 919
 920
 921

Fig. 14. Upper panel: ice crystal habit distribution assumed for MODIS Collection 5 ice cloud property retrieval. Middle panel: comparison of the phase functions of smooth and

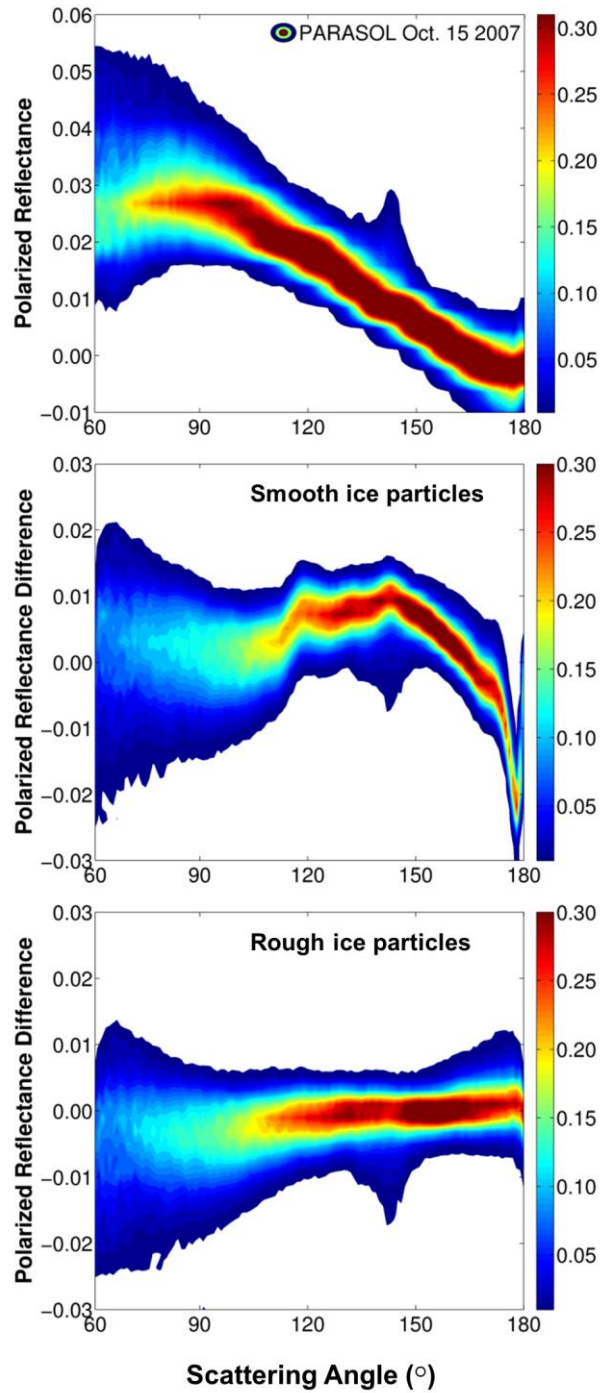
922 roughened ice crystals with an effective particle size of 50 μm based on the habit
923 distribution in the upper panel, and the phase matrix element ratio $-P_{12}/P_{11}$
924 corresponding to the phase functions in the middle panel.

925

926

927

928



929

930

931 Fig. 15. Upper panel: density contours of polarized reflectance measurements at 865 nm

932 from the PARASOL satellite on 15 October 2007. Over 60,000 pixels over the ocean are

933 included, corresponding to approximately 866,000 total viewing geometries plotted.

934 Middle panel: the difference between simulated polarized reflectance and measured
935 polarized reflectance for each viewing geometry. The MODIS collection 5 habit
936 distribution and smooth ice particles with an effective diameter of 50 μm were used in the
937 simulation, and the optical depth was 5. Lower panel: the difference in polarized
938 reflectance using C5 with severely roughened ice particles and all simulation parameters
939 the same as the middle panel.

940